Università degli Studi di Napoli
Federico II

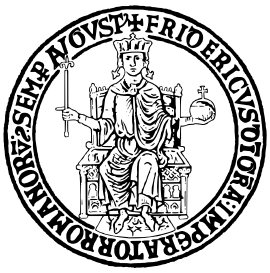

Dipartimento di Ingegneria Elettrica e delle Tecnologie dell'Informazione

Classe delle Lauree Magistrali in Ingegneria Elettronica, Classe n. LM-29

Corso di Laurea Magistrale in Ingegneria Elettronica

Tesi di Laurea

Optical measurement system automatization based on Autocollimator for tiny bent silicon crystals

Relatori
Ch.mo Prof. Pasquale Arpaia
Dr. Roman Gozdur

Candidato
Stefano Di Gennaro
M61/870

Correlatori
Dr. Walter Scandale
Dr. Antonio Esposito

Anno Accademico
2024/2025

Abstract

The use of bent crystals in high-energy particle accelerators makes it possible to exploit several physical phenomena, such as *channeling* and *volume reflection*, to steer particles toward a desired location. Collimation, steering toward absorbers, extraction, and the *merging* of two extracted beams are among the goals enabled by beam interactions with silicon crystals. To achieve these objectives, an accurate and reliable characterization of the curvature of bent crystals is required. Within the framework of the UA9 experiment at CERN, the precise measurement of both the primary and the anticlastic curvature components is essential to the success of each experiment, as it helps avoid numerous trial bending attempts and saves valuable beam time, while also ensuring the reproducibility of experimental results.

This thesis presents the development and validation of an automated optical measurement system based on an autocollimator for the characterization of tiny bent silicon crystals. After a review of the physical principles governing particle–crystal interactions and of the existing techniques for crystal curvature measurements, a detailed description of the autocollimator operating principle and of the adopted experimental setup is provided.

Dedicated measurement procedures and image processing algorithms are developed for different crystal geometries, including thin strip crystals and RD22 crystals. The system combines motorized translation stages with custom software for automated data acquisition and processing, enabling systematic and repeatable angular mapping of the crystal surface. In order to enhance measurement accuracy, signal processing techniques such as Principal Component Analysis and Savitzky–Golay filtering are employed. The former enables the estimation of the principal component of the data distribution and, consequently, the determination of the central value of that distribution, while the latter is applied to estimate the curvature trend, reducing the influence of measurement noise

and preventing spurious local oscillations from affecting the curvature estimation.

The obtained curvature measurements are compared with reference beam-based measurements performed in the CERN SPS North Area. The results demonstrate that the proposed optical system provides reliable estimates of both primary and anticlastic curvature, with a precision compatible with the requirements of crystal-assisted collimation studies.

The system provides primary curvature radii for strip crystals with deviations below 7% for Strip 1 and within 10% for Strip 2, and relative standard uncertainties below 4%. The anticlastic curvature angles measured on strip crystals are consistent with beam-based reference values within $\pm 22\,\mu$rad, with a standard uncertainty of $6\,\mu$rad. For RD22 crystals, the central anticlastic curvature measured by the automated system differs from beam measurements by less than 5%, demonstrating good consistency with in-beam characterization and confirming the reliability of the proposed laboratory method. Furthermore, the anticlastic curvature gradient of an RD22 crystal is captured with good agreement with the beam-based profile: over the common span $x \in [-9, 9]$ mm, the difference between the two parabolic fits shows a bias of $-6.01\,\mu$rad, an RMS deviation of $8.29\,\mu$rad, and a maximum absolute deviation of $15.69\,\mu$rad.

The developed approach represents a flexible and efficient laboratory tool for crystal pre-characterization and quality control, reducing the dependence on resource-intensive beam tests.

Sommario

L'utilizzo di cristalli piegati negli acceleratori di particelle ad alta energia permette di sfruttare vari fenomeni fisici, quali *channeling* e *volume reflection*, per direzionare le particelle verso la destinazione desiderata. Collimazione, indirizzamento verso assorbitori, estrazione e *merging* di due fasci estratti sono tra gli obiettivi resi possibili dalle interazioni tra fascio e cristalli di silicio. Affinché tali obiettivi siano raggiungibili, è richiesta una caratterizzazione accurata e affidabile della curvatura dei cristalli piegati. Nell'ambito dell'esperimento UA9 al CERN, la misura precisa sia della componente di curvatura primaria sia di quella anticlastica è essenziale per la buona riuscita di ogni esperimento, consentendo di evitare numerosi tentativi di piegatura e di risparmiare tempo di fascio, nonché di garantire la riproducibilità dei risultati sperimentali.

Questa tesi presenta lo sviluppo e la validazione di un sistema automatizzato di misura ottica, basato su un autocollimatore, per la caratterizzazione di piccoli cristalli di silicio piegati. Dopo una rassegna dei principi fisici che governano l'interazione tra particelle e cristalli e delle tecniche esistenti per la misura della curvatura dei cristalli, viene fornita una descrizione dettagliata del principio di funzionamento dell'autocollimatore e dell'apparato sperimentale adottato.

Vengono sviluppate procedure di misura dedicate e algoritmi di elaborazione delle immagini per differenti geometrie di cristallo, includendo cristalli a lamina sottile (strip) e cristalli RD22. Il sistema combina stadi di traslazione motorizzati con software personalizzato per l'acquisizione e l'elaborazione automatica dei dati. Per migliorare l'accuratezza delle misure, vengono impiegate tecniche di elaborazione del segnale quali l'Analisi delle Componenti Principali (Principal Component Analysis, PCA) e il filtraggio di Savitzky–Golay. La prima consente di stimare la componente principale della distribuzione dei dati e, di conseguenza, di determinarne il valore centrale, mentre il secondo viene applicato per stimare l'andamento della curvatura, riducendo

l'influenza del rumore di misura e impedendo che oscillazioni locali spurie influenzino la stima della curvatura.

Le misure di curvatura ottenute vengono confrontate con misure di riferimento basate su fascio, eseguite presso la North Area dello SPS del CERN. I risultati dimostrano che il sistema ottico proposto fornisce stime affidabili sia della curvatura primaria sia di quella anticlástica, con una precisione compatibile con i requisiti degli studi sulla collimazione assistita da cristalli.

Il sistema fornisce raggi di curvatura primari per cristalli a strisce con scostamenti inferiori al 7% per Strip 1 e entro il 10% per Strip 2, e incertezze standard relative inferiori al 4%. Gli angoli di curvatura anticlastica misurati sui cristalli a strisce sono coerenti con i valori di riferimento basati su fascio entro $\pm 22\,\mu$rad, con un'incertezza standard di $6\,\mu$rad. Per i cristalli RD22, la curvatura anticlastica centrale misurata dal sistema automatizzato differisce dalle misure su fascio di meno del 5%, mostrando una buona consistenza con la caratterizzazione in fascio e confermando l'affidabilità del metodo di laboratorio proposto. Inoltre, il gradiente di curvatura anticlastica di un cristallo RD22 risulta in buon accordo con il profilo ricostruito da fascio: nell'intervallo comune $x \in [-9, 9]$ mm, la differenza tra i due fit parabolici presenta un bias di $-6.01\,\mu$rad, un valore RMS di $8.29\,\mu$rad e uno scostamento massimo di $15.69\,\mu$rad.

L'approccio sviluppato rappresenta uno strumento di laboratorio flessibile ed efficiente per la pre-caratterizzazione e il controllo qualità dei cristalli, riducendo la dipendenza da test su fascio, onerosi in termini di risorse.

Contents

Introduction

The European Organization for Nuclear Research (CERN) is the world's leading laboratory for particle physics and accelerator science [1]. Located on the border between France and Switzerland, near Geneva, CERN operates a unique and complex chain of particle accelerators, that serve both fundamental research in high energy physics and advanced studies in beam dynamics, accelerator technologies, and radiation–matter interaction. Over the decades, CERN has progressively developed an accelerator infrastructure capable of accelerating and manipulating particle beams with unprecedented energy and intensity. This infrastructure enables not only the exploration of the fundamental constituents of matter, but also the investigation of novel beam manipulation techniques that are essential for the safe and efficient operation of modern hadron colliders.

The CERN accelerator complex, illustrated in figure 1, is organized as a sequence of machines that gradually increase the beam energy and quality before injection into flagship facilities. Protons are generated and initially accelerated in linear accelerators and booster synchrotrons, before being transferred to the Super Proton Synchrotron (SPS), which plays a central role both as an injector for the Large Hadron Collider (LHC) and as a versatile experimental machine. The SPS can store high intensity proton and ion beams at energies up to several hundreds of GeV and provides a unique environment for accelerator physics experiments. Its flexible optics, extensive instrumentation, and access to dedicated experimental regions make it particularly suitable for testing novel beam control concepts under realistic operational conditions.

The Large Hadron Collider represents the most demanding operational environment within the CERN complex. With TeVs beam energies and extremely high stored beam power, the LHC requires an exceptionally efficient and reliable collimation system to protect superconducting magnets and experimental detectors from beam losses. Beam

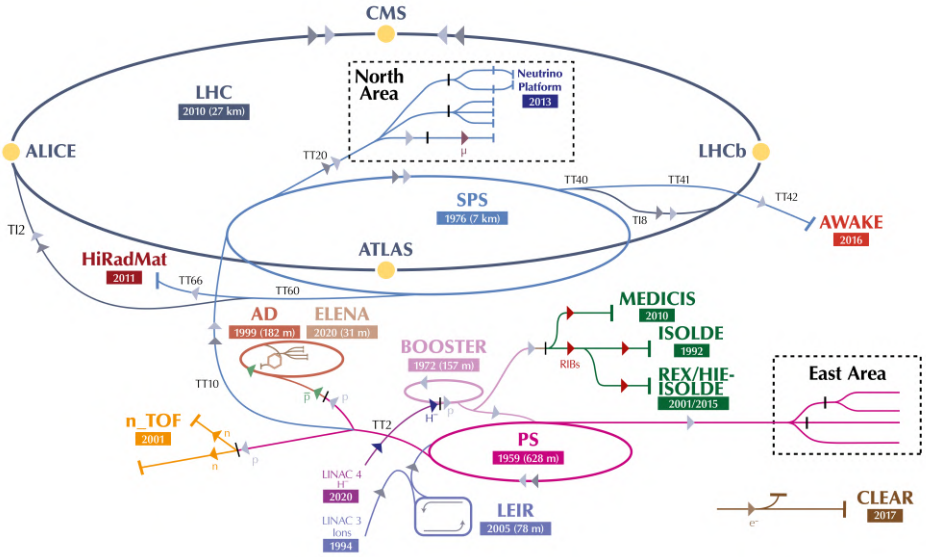

Figure 1: CERN Accelerator complex

halo particles, generated by diffusion processes and beam–beam effects [2], must be intercepted and absorbed in a controlled manner. Even small inefficiencies in the cleaning system can lead to excessive radiation loads, quenches of superconducting magnets, or damage to sensitive components. For this reason, the optimization of beam collimation is a critical aspect of LHC performance and of future high luminosity collider upgrades [3].

Conventional collimation systems rely on a multi stage approach, in which a primary collimator made of amorphous material increases the angular divergence of halo particles through multiple Coulomb scattering, allowing downstream absorbers to intercept them at larger impact parameters. While effective, this approach intrinsically produces significant secondary particle fluxes and requires many beam passages before efficient absorption occurs. As beam energy and intensity increase, these limitations become increasingly relevant. This has motivated the exploration of alternative concepts capable of providing larger and more deterministic angular deflections with reduced generation of secondary radiation.

In this context, the use of bent crystals as primary collimation elements has emerged as a promising experimental solution [4]. When a charged particle enters a crystalline lattice at a sufficiently small angle with respect to its atomic planes, it can be trapped in channeling states and guided by the averaged electromagnetic potential of the crystal

[5]. If the crystal is bent, channeled particles follow the curvature of the lattice planes and experience a coherent deflection equal to the crystal bending angle. Particles that do not fulfill the channeling conditions may still undergo coherent interactions such as volume reflection, leading to a well defined angular kick opposite to the crystal curvature [6]. These effects provide the possibility of steering halo particles in a controlled way, directing them deep into downstream absorbers and significantly reducing uncontrolled losses. A detailed feasibility study of crystal assisted collimation for the LHC, including multi turn Monte Carlo simulations and optimization of crystal parameters, was presented in [7], where a significant reduction of the halo intensity with respect to conventional amorphous collimation systems was predicted.

The experimental validation of crystal assisted collimation in circular accelerators is the primary objective of the UA9 Collaboration. UA9 was established in 2010 to investigate, under realistic accelerator conditions, the feasibility and performance of bent crystal collimation for high energy hadron beams [8]. Crystals of various shapes are studied using high-energy beams of hadrons or leptons for different purpose like crystal collimation, beam extraction, reducing hardware irradiation, and beam merging. The collaboration operates dedicated experimental setups within the CERN accelerator complex, with emphasis on the H8 beam line at SPS North Area as a testbed.

The UA9 experiment exploits both extracted and circulating beams in the SPS to study crystal–beam interactions and collimation performance. In the SPS ring, bent silicon crystals are installed on high precision goniometers, allowing angular alignment with microradian accuracy. This level of control is essential, since channeling and volume reflection phenomena occur within very small angular acceptances that decrease with increasing beam energy. The experimental layout is complemented by a set of beam loss monitors, scintillators, and other radiation detectors that provide a direct measurement of loss patterns and background reduction when the crystal is properly aligned.

One of the distinctive features of the UA9 program is its strongly experimental approach. Rather than relying solely on simulations or idealized models, the collaboration performs systematic measurements of beam losses, angular scans, and alignment procedures with stored beams. UA9 has developed dedicated experimental setups in the SPS

North Area to characterize individual crystals using extracted beams. These measurements allow precise reconstruction of particle trajectories through bent crystals using high resolution silicon strip detectors. Such studies are crucial to quantify channeling efficiency, dechanneling length, volume reflection angles, and the impact of crystal imperfections. The combination of single pass measurements and multi turn collimation tests forms a coherent experimental strategy, linking microscopic crystal–particle interaction mechanisms to macroscopic accelerator performance.

The results obtained by the UA9 Collaboration over more than a decade of operation have played a key role in establishing bent crystals as viable operational devices in modern accelerators. Crystal assisted collimation concepts developed and validated in the SPS have been successfully extrapolated to the LHC, where bent crystals have been installed and tested under operational conditions. These achievements demonstrate that coherent interactions in crystals are not only a subject of fundamental interest, but also a practical tool for beam control in high energy accelerators.

1 Fundamentals of bent crystals and curvature measurements

This chapter introduces the fundamental concepts required to understand the behaviour and use of bent silicon crystals for beam manipulation. It briefly reviews crystal structure and orientation, with emphasis on silicon and Miller indices, describes the main coherent particle–crystal interaction regimes (planar and axial channeling, dechanneling, volume capture and volume reflection), and explains how macroscopic bending and anticlastic effects modify the lattice and impact beam dynamics. The chapter concludes with an overview of the principal techniques used to measure crystal curvature: beam-based deflection reconstruction, X-ray Bragg diffraction, and optical surface profilometry, which together provide the experimental basis for the optical autocollimator method developed later in this thesis.

1.1 Crystals and principle of operation

The use of bent crystals for beam manipulation relies on the ordered structure of crystalline solids and on the coherent interaction between charged particles and the periodic electric fields generated by the crystal lattice. A proper understanding of the crystal structure, of the underlying physical mechanisms governing particle–crystal interactions, and of the methods used to characterize crystal curvature is therefore essential for the interpretation of experimental results and for the optimization of crystal-based devices.

1.1.1 Crystal structure

A crystal is a solid in which atoms are arranged in an ordered and symmetric structure [9]. This geometrical arrangement is called the *crystal lattice*, and it is usually rep-

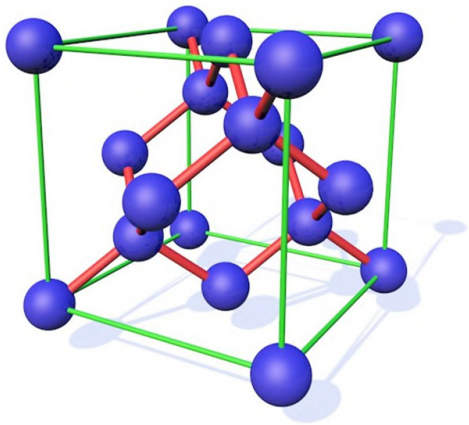

Figure 1.1: Diamond-cubic crystal structure of silicon, showing the tetrahedral bonding arrangement and the unit cell.

resented by a spatial grid of straight lines whose intersection points are called *lattice nodes*. Not every lattice node necessarily corresponds to the position of an atom.

Within the lattice, it is possible to identify a minimum volume that, by periodic repetition, generates the entire structure. This volume contains a group of atoms, referred to as the *basis*, and together with the lattice vectors defines the *unit cell*. The unit cell can therefore be regarded as the fundamental building block of the crystal.

One may choose an arbitrary origin in the lattice, from which a generic position vector $\mathbf{r}$ can be written as

$$\mathbf{r} = u_1\mathbf{a} + u_2\mathbf{b} + u_3\mathbf{c},$$

where u_1, u_2 and u_3 are real coefficients, and $\mathbf{a}$, $\mathbf{b}$ and $\mathbf{c}$ are the primitive lattice vectors, which in the simplest case are mutually orthogonal.

Crystal lattices can be classified in several different ways, depending on their symmetry and geometry. A detailed classification is beyond the scope of this thesis; however, a structure of particular interest for the following discussion is that of silicon (Si). Silicon crystallizes in the diamond-cubic structure, shown in Figure 1.1.

In addition to atomic positions, it is necessary to introduce a systematic way to identify the orientation of planes within a crystal. The most commonly used convention to label crystal planes is the *Miller index system*. In this notation, a plane is identified by three integers (hkl), known as the Miller indices, expressed in units of the lattice parameters.

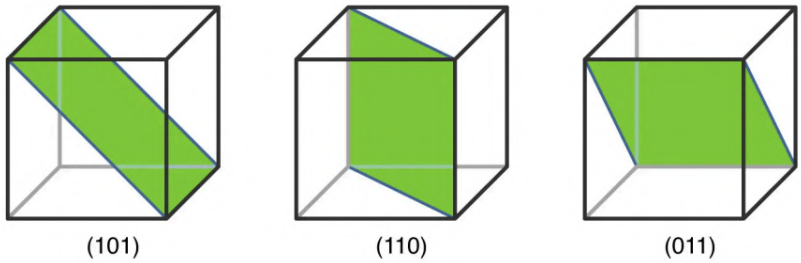

Figure 1.2: Examples of crystallographic planes in a cubic lattice, labeled by their Miller indices.

Planes characterized by the same Miller indices are parallel to each other and are physically equivalent within the crystal lattice. Therefore, the notation (hkl) does not refer to a single plane but to a family of equally spaced parallel planes. Figure 1.2 shows three examples of crystallographic planes and their Miller indices.

As mentioned in the introduction, the UA9 experiment uses bent crystals, in which the crystallographic planes follow the macroscopic curvature of the sample [10]. In such crystals, a cross-section of a crystallographic plane is curved rather than straight, and the lattice planes locally conform to the applied macroscopic bending.

The bending of a crystal used for beam manipulation must satisfy two key requirements: preservation of crystalline order at the atomic scale and generation of a controlled curvature of the lattice planes. For silicon crystals, this is achieved by applying elastic stress well below the fracture limit, ensuring that the deformation remains reversible and does not introduce significant lattice defects.

The bending angle θ_b imparted to a particle traversing the full crystal length is

$$\theta_b = \frac{L}{R}.$$

When a crystal is bent to produce the desired longitudinal curvature, the elastic response of the solid generally gives rise to a secondary, transverse curvature known as anticlastic curvature. This effect occurs because longitudinal bending induces transverse strains through the material's elastic response (commonly described in continuum mechanics via the Poisson effect): as the crystal is curved in the primary direction, a curvature of

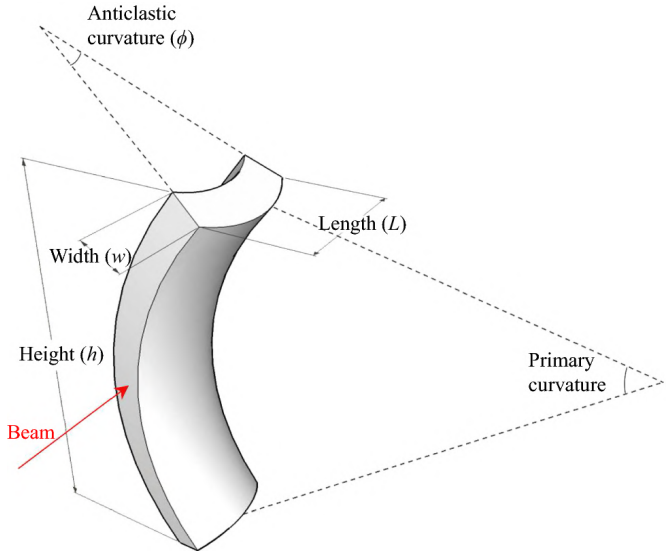

Figure 1.3: Schematic of anticlastic curvature and beam direction highlighted

opposite sign typically appears in the perpendicular direction [11]. The exact magnitude and spatial distribution of the anticlastic component depend on the crystal geometry and the boundary conditions imposed by the mount, and can become significant for thin samples or for holders that do not rigidly constrain the edges. Experimentally, anticlasticity leads to a systematic variation of the lattice-plane orientation across the crystal width and can introduce apparent torsion or non-uniform bending that affect beam-based deflection measurements, X-ray rocking-curve maps and optical autocollimator readings. Therefore, a complete characterization includes transverse curvature components or, preferably, a surface angular map in addition to the nominal longitudinal radius. A schematic of the anticlastic effect is shown in Figure 1.3.

Typical bending angles used in collimation and extraction experiments range from a few microradians to milliradians, depending on beam energy and optical constraints.

1.1.2 Particle–crystal interaction

When a charged particle enters a crystal at a small angle with respect to a family of crystallographic planes, its transverse dynamics is governed by the averaged planar potential generated by the periodic arrangement of atomic planes. This description traces back to the seminal formulation of the continuum model by Lindhard [5]. Within the continuum approximation, the discrete atomic structure is replaced by an effective one-

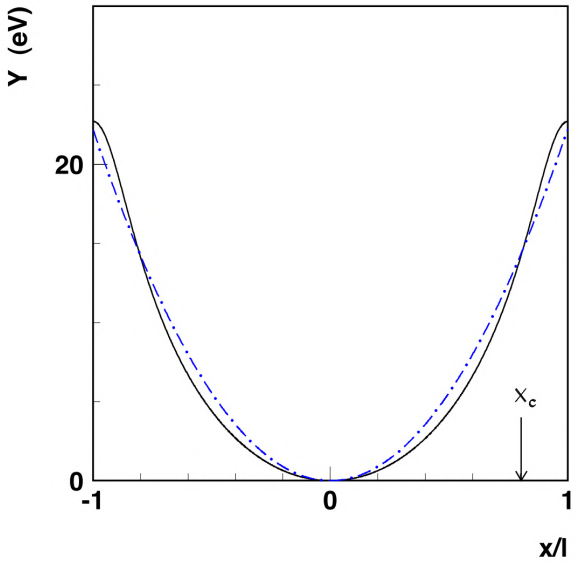

Figure 1.4: Averaged planar potential for the (110) channel in silicon at room temperature. The dashed curve represents the parabolic approximation. The transverse coordinate x is measured from the channel center; l denotes the half interplanar spacing, $x_c = l - r_c$ is the maximum stable oscillation amplitude for channeled particles, and r_c is the critical distance from the channel walls [12].

dimensional potential $U(x)$, where x denotes the transverse distance from the plane. In the continuum approximation introduced by Lindhard [5], the discrete atomic potentials are averaged along the longitudinal direction of motion, leading to a continuous planar potential obtained by summing the contributions of all lattice planes. For a family of equally spaced planes with interplanar distance d_p, the averaged potential can be written as

$$\overline{U}(x) = \sum_{n=-\infty}^{+\infty} U_1(x - nd_p), \tag{1.1}$$

where $U_1(x)$ is the potential of a single atomic plane averaged over the atomic positions. The figure 1.4 represents the avaraged planar potential.

Depending on the alignment of the incident beam with the crystal lattice, channeling can occur either in the axial or planar regime, corresponding to alignment with major crystallographic axes or planes, respectively [13]. The inverse process, known as dechanneling (DC), may take place in both straight and bent crystals. Additional coherent effects arise specifically due to crystal bending, most notably volume capture (VC) and volume reflection (VR). A comprehensive treatment of these relations and

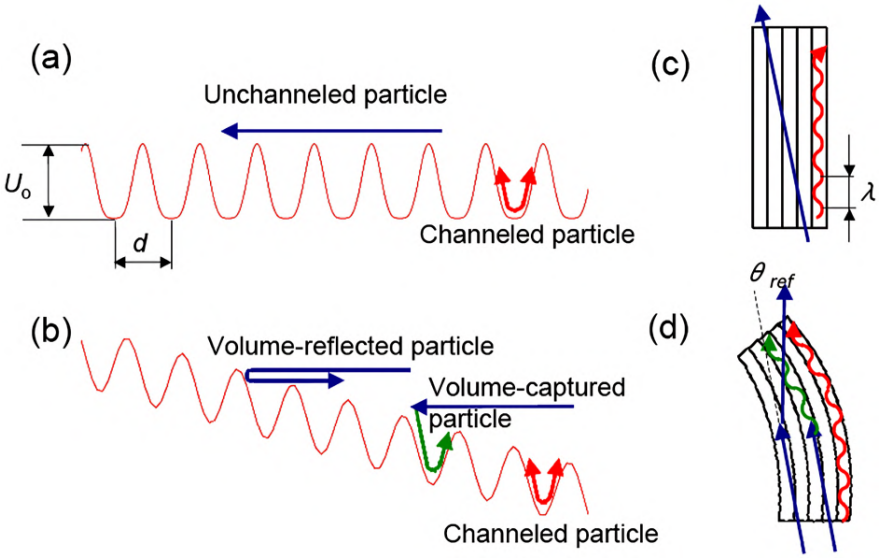

Figure 1.5: Schematic representation of coherent particle–crystal interactions in straight and bent crystals, adapted from Ref. [14]. (a) Periodic planar potential in a straight crystal for positively charged particles, showing a channeled particle undergoing oscillatory motion and an unchanneled particle with transverse energy exceeding the potential barrier U_0. (b) Effective planar potential in a bent crystal, illustrating volume reflection, volume capture, and channeling. (c) and (d) Corresponding particle trajectories in straight and bent crystals, respectively, highlighting the characteristic deflection angle associated with volume reflection. [14]

their extension to bent crystals can be found in [12].

A schematic representation of these interaction regimes is shown in Fig. 1.5. In straight crystals, particles with transverse energy below the planar potential barrier are confined between adjacent planes and undergo oscillatory motion, while particles with larger transverse energy remain unchanneled. In bent crystals, the curvature modifies the effective potential, enabling volume reflection, where particles are coherently deflected by the bent planar potential, and volume capture, where particles are trapped into the channeling regime inside the crystal volume. These processes constitute coherent interactions, as the particle experiences the collective effect of the ordered atomic structure rather than incoherent scattering from individual atoms [14].

Planar channeling

Channeling occurs when the transverse energy of the particle,

$$E_\perp = \frac{pv\theta^2}{2} + U(x),$$

is smaller than the height of the interplanar potential barrier. In this regime, the particle is trapped between adjacent planes and performs oscillatory motion while propagating along the crystal. The maximum entrance angle for channeling is given by the critical angle

$$\theta_c = \sqrt{\frac{2U_0}{pv}},$$

where U_0 is the depth of the planar potential well, p the particle momentum and v its velocity. The critical angle is the incidence angle at which the particle's transverse kinetic energy does not exceed the channel's potential barrier near the edge of the channel (i.e., for x close to the channel semi-length). Equivalently, it is the largest angle for which the transverse energy remains below the maximum potential energy, so that channeling can still occur.

In a bent crystal, channeling remains possible as long as the centrifugal force in the bent reference frame does not exceed the maximum restoring force of the planar potential. This defines a critical curvature radius R_c, below which channeling is suppressed. For $R \gg R_c$, channeled particles follow the bent planes and are deflected by the bending angle θ_b.

Dechanneling

Dechanneling refers to the process by which a channeled particle exits the channel due to incoherent interactions with lattice atoms, mainly via multiple scattering. The probability of remaining channeled decreases approximately exponentially with penetration depth z:

$$P_{\mathrm{ch}}(z) = \exp\!\left(-z/L_d\right),$$

where L_d is the dechanneling length. The dechanneling length depends on particle energy, crystal orientation and bending radius, and typically increases with beam energy.

Volume capture

Volume capture can be considered as the inverse process of dechanneling. A particle initially moving above the potential barrier can lose transverse energy through scattering

and become trapped in a channel inside the crystal bulk. Although the probability of volume capture in a single passage is small, it can play a role in multi-turn dynamics in circular accelerators, where particles may interact repeatedly with the crystal.

Volume reflection

Volume reflection occurs when particles traverse a bent crystal at angles larger than the channeling acceptance but still interact coherently with the bent potential. In this case particles are not trapped but are smoothly deflected by the collective field of the bent planes, receiving a small angular kick opposite to the bending direction. The volume-reflection angle is typically of the order of a few microradians and is weakly dependent on the exact alignment, making the effect intrinsically robust.

Volume reflection is characterized by nearly 100% efficiency for particles interacting with the crystal, at the expense of a smaller deflection angle compared to channeling. For this reason it is particularly attractive when angular stability is more important than maximum deflection.

Axial and quasi-axial channeling

In addition to planar effects, coherent interactions can occur when the particle direction is aligned with a major crystallographic axis. In axial channeling, the particle is confined by the combined potential of several atomic strings, leading to strong focusing and a very small angular acceptance. Because the axial potential is complex and highly sensitive to alignment, pure axial channeling is rarely exploited for collimation applications.

More commonly, particles interact in a quasi-axial regime, where the beam is near a crystal axis but not perfectly aligned. In this case, planar and axial fields combine, modifying the effective potential and enhancing processes such as volume capture and dechanneling. Quasi-axial effects are observed experimentally as broader angular structures surrounding the planar channeling region.

Amorphous and incoherent interactions

When the crystal orientation does not satisfy the conditions for coherent effects, the crystal behaves effectively as an amorphous material. In this regime particle deflection is dominated by incoherent multiple Coulomb scattering and by nuclear interactions. This amorphous-like behavior provides a reference baseline and is always present as a competing process, even when coherent effects dominate.

Depending on crystal orientation and beam parameters, particles interacting with a bent crystal may undergo planar channeling, axial or quasi-axial channeling, volume reflection, volume capture, dechanneling, or purely incoherent scattering. The coexistence of these regimes is a defining feature of bent-crystal operation in realistic accelerator environments and must be carefully accounted for in experimental interpretation and simulation studies.

Depending on the crystal orientation with respect to the incoming beam, different regimes dominate: channeling near perfect alignment, volume reflection at larger angles, and amorphous-like scattering when coherent conditions are not satisfied. The coexistence of these processes is a defining feature of bent-crystal operation in realistic accelerator environments and must be accounted for in both experimental interpretation and simulation studies.

1.2 Crystal curvature measurements

The following paragraph analyze the crystal curvature measurement obtained in other ways respect to the use of the autocollimator, deeply faced in the next chapter. The first one is the characterization by the beam particle during the last experiment of UA9 in the H8 beam line of the CERN-SPS North Area, the second one is the curvature evaluation thanks to x-rays Bragg diffraction and the last one is the curvature evaluation through optical surface profilometry.

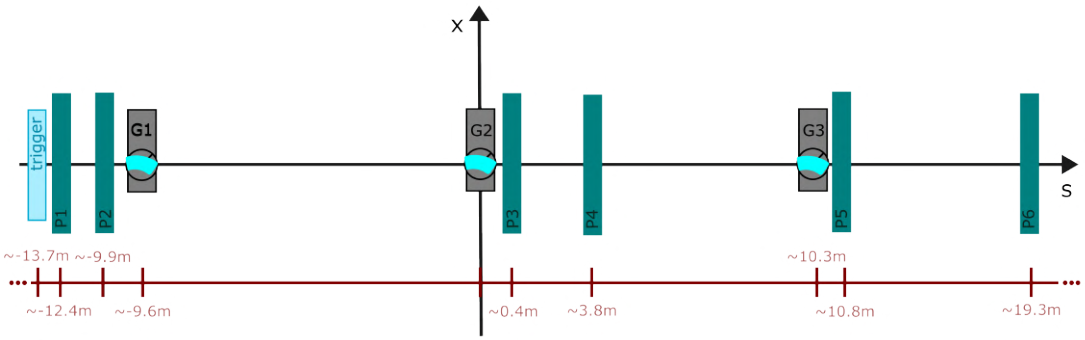

Figure 1.6: UA9 layout of the H8 experimental area for the merging test [15].

1.2.1 Beam curvature assessment

During the most recent data-taking run on the H8 beam line, the crystals were positioned to extract two converging beams using two bent crystals and then to merge these extracted beams into a resulting beam with an intensity close to the sum of the incoming particles [15]. For this reason, the UA9 installation layout follows the arrangement illustrated in Figure 1.6. As shown there, six silicon-strip detectors (P1–P6) and three goniometer assemblies hosting the bent crystals are installed. The impact points recorded on detectors P1–P6 are fitted to reconstruct particle trajectories.

Figure 1.7 illustrates the trajectory reconstruction: two measurement planes upstream of the crystal and two downstream are required to reconstruct the full particle trajectory. The crystal curvature is then evaluated from the deflection angle experienced by channeled particles, i.e., the angle between the incoming and outgoing trajectory segments for particles undergoing channeling.

In practice, for each particle crossing the experimental setup, straight-line fits are performed independently on the upstream and downstream track segments, using the hits recorded by the silicon-strip detectors. The angular difference between these two reconstructed segments provides a direct measurement of the particle deflection induced by the crystal. By selecting only particles in the channeling regime, identified through their characteristic deflection and reduced angular spread, the mean deflection angle can be extracted with high precision.

Assuming that the crystal bending radius is sufficiently large to ensure stable channeling conditions, the measured deflection angle can be directly related to the crystal curvature

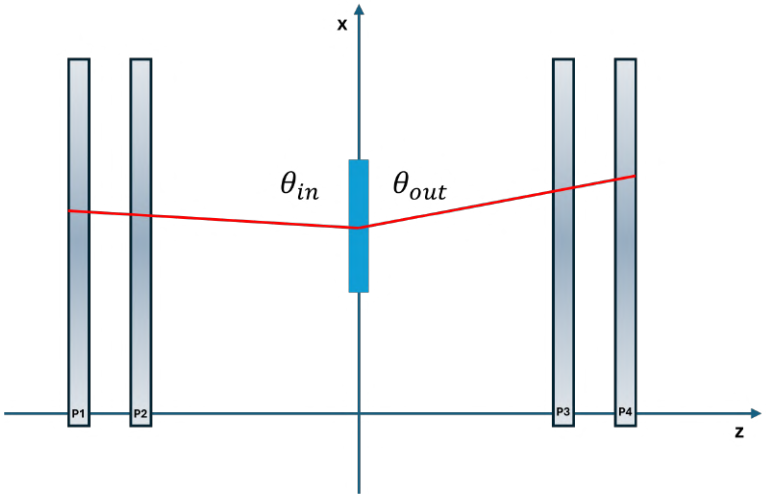

Figure 1.7: Tracks reconstruction of the particles passing through the crystal.

through purely geometrical considerations. In particular, the curvature radius R is obtained from the ratio between the crystal length L along the beam direction and the average channeling deflection angle θ_b, according to $R = L/\theta_b$. This method provides an effective, beam-based determination of the crystal curvature under actual operating conditions, including possible non-uniformities (torsion) induced by mounting stresses or holder imperfections.

An important advantage of this technique is that it probes the crystal curvature in situ, i.e., under the same mechanical and thermal conditions experienced during beam operation. However, the measurement accuracy is ultimately limited by the spatial resolution of the tracking detectors, multiple Coulomb scattering in the material, and the intrinsic angular divergence of the beam.

In the following of this thesis, the beam-based curvature evaluation will be considered as the reference measurement used to calibrate and validate the new optical curvature measurement system based on the autocollimator. For this reason, it represents the benchmark against which the performance and accuracy of the optical method will be assessed. This approach has been extensively adopted within the UA9 collaboration for the characterization of bent crystals during beam tests, allowing robust conclusions to be drawn, which will be discussed in greater detail in the following sections.

1.2.2 X-ray Bragg diffraction procedure

In addition to beam-based methods, which is a method of measurement that consumes high resources and is only accessible when a facility is available, a well-established and widely adopted technique for the characterization of bent crystals is based on X-ray Bragg diffraction. X-ray diffraction methods provide a non-destructive, high-precision probe of the crystal lattice and allow the curvature of crystallographic planes to be measured directly through their angular misorientation, thanks to the diffraction effect which occurs between X-ray photons and atomic planes in specific geometrical conditions [16]. These techniques have been extensively used both for slightly bent crystals and for warped silicon wafers, and they are particularly well suited for laboratory characterization prior to beam tests.

The key advantage of X-ray-based techniques lies in their sensitivity to the local orientation of lattice planes, enabling not only the determination of an average curvature radius but also the mapping of spatial variations of curvature and strain across the crystal surface. This capability is essential for identifying non-uniform bending, torsion, or local defects introduced during crystal fabrication or mounting.

X-rays are electromagnetic radiation with wavelengths comparable to the interplanar spacing of crystalline solids, typically of the order of a few ångströms. When an incident X-ray beam interacts with a crystal, constructive interference of the scattered waves occurs only for specific incidence angles, according to the Bragg condition

$$2d_{hkl} \sin\theta = n\lambda,$$

where d_{hkl} is the spacing between crystallographic planes identified by the Miller indices (hkl), θ is the Bragg angle, λ is the X-ray wavelength, and n is an integer diffraction order. For a perfect, flat crystal, this condition is satisfied simultaneously over the entire illuminated region when the crystal is set at the appropriate angle.

In a bent crystal, however, the local orientation of the lattice planes varies as a function of position along the crystal. As a consequence, the Bragg condition is satisfied at different incidence angles for different points on the sample. This effect manifests itself

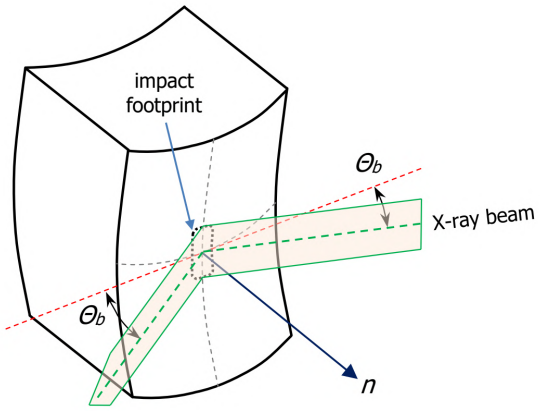

Figure 1.8: Determination of normal n to crystal area labelled "impact footprint" where X-ray diffraction occurs at Bragg angle θ_b [17].

as a position-dependent shift of the diffraction peak in so-called rocking curves, i.e. the diffracted intensity measured as a function of the crystal rotation angle. By measuring how the Bragg angle varies with position on the crystal, the curvature of the diffracting planes can be directly inferred.

The angular orientation of the crystal, considered as the normal vector n to this surface fragment, is measured when the angle of the desired atomic plane corresponds to a Bragg diffraction angle θ_b relative to the X-ray beam, as shown in figure 1.8 [17].

The schematic diagram for measuring the radius of curvature of a crystal (neglecting dispersive effects in the simplest case) is shown in figure 1.9. Points A and B indicate two positions on the sample; the corresponding diffracted beam positions on the one-dimensional detector are X_1 and X_2. If the crystal is bent and the Bragg condition is satisfied first at position A, then by rotating the crystal in small angular steps the Bragg condition will be satisfied successively from A to B. The rotation angle ω between positions is obtained from the difference in the angular coordinates extracted from the contour map; in practice the difference $\Delta Y = Y_2 - Y_1$ on the contour map is converted to an angular rotation by the experimental angular calibration.

From simple circular-arc geometry, the radius of curvature R is related to the chord length D (the distance between sample positions A and B) and the subtended angle ω by the relation

$$R = \frac{D}{2\sin(\omega/2)}. \tag{1.2}$$

Thus, measurement of the chord D together with the rotation angle ω determines the curvature radius.

In a realistic (dispersive) experimental geometry an angular correction β due to the monochromator dispersion must be taken into account. Denoting the measured angular difference (from the contour map and detector geometry) by ω_{meas}, the effective rotation to use in equation (1.2) is

$$\omega \;=\; \omega_{\text{meas}} - \beta,$$

where β is computed from the monochromator and beamline parameters (wavelength spread, monochromator asymmetry factors, beam width at the monochromator, etc.). Once β is evaluated for the given setup, the corrected radius is obtained from equation (1.2).

Practical notes on obtaining the inputs:

- The chord length D can be measured directly on the sample (mechanical coordinates) or inferred from the known step size between measurement positions.
- The measured angular difference ω_{meas} is derived from detector observables (pixel shifts $\Delta X = X_2 - X_1$ and/or contour-map differences ΔY) using the instrument angular calibration. For small angles, pixel shifts can be converted to scattering angles via $\Delta\theta \approx \Delta X \cdot p/L$, where p is the pixel pitch and L is the sample-to-detector distance.
- The dispersion correction β depends on monochromator parameters (wavelength spread $\Delta\lambda/\lambda$, asymmetry factors b_1, b_2, and incident-beam width S); its exact expression depends on the monochromator geometry and should be applied according to the beamline calibration or the formula provided by the monochromator model.

A positive value of R indicates concave bending (with respect to the incident beam), while a negative value indicates convex bending, according to the chosen sign convention.

The results reported in the cited studies demonstrate that X-ray diffraction methods are capable of resolving both uniform curvature and local variations across the crystal.

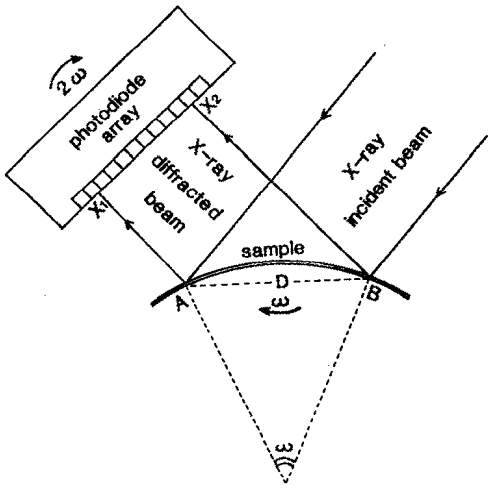

Figure 1.9: Schematic diagram of the principle for measuring the radius of curvature of a crystal [18].

In particular, curvature radii measured with this technique were found to be in good agreement with independent determinations obtained using conventional double-crystal diffractometry, while providing additional spatially resolved information [17]. Furthermore, X-ray diffraction mapping has been successfully applied to quantify warpage and non-uniform strain in silicon wafers, highlighting its robustness and versatility for crystal metrology [19].

For bent crystals used in beam manipulation experiments, X-ray Bragg diffraction therefore represents a powerful complementary tool to beam-based measurements. While it does not probe the crystal under actual beam operating conditions, it provides a precise and detailed characterization of the lattice curvature and its uniformity, which is essential for the success of the experiments.

1.2.3 Optical surface profilometry

In addition to beam-based and X-ray diffraction techniques, the curvature of bent silicon crystals can be characterized by direct optical measurements of the crystal surface profile. Optical surface profilometry provides a non-contact, high-precision method to reconstruct the macroscopic shape of the crystal and to extract its curvature through geometrical analysis of the measured surface.

In the context of bent crystals for beam manipulation, optical profilometry is particularly useful as a fast laboratory technique for pre-characterization and quality control. By measuring the external surface of the crystal with micrometric or sub-micrometric resolution, it is possible to assess the uniformity of the applied bending and to identify macroscopic distortions such as non-uniform curvature, torsion, or edge effects induced by the mounting procedure.

A widely used instrument for this purpose is the *AltiSurf 520* optical profilometer, developed by Altimet [20]. The AltiSurf 520 is designed for high-precision three-dimensional surface metrology of silicon wafers and optical components, combining motorized positioning stages with interchangeable optical sensors. Owing to its flexibility in scan length and resolution, this system is well suited for the characterization of bent silicon crystals over the full crystal length.

The AltiSurf 520 is routinely employed by AlpyX, the company supplying bent silicon crystals for UA9 and related experiments. AlpyX is based in Grenoble, France, and specializes in the fabrication of high-quality silicon crystals [21]. The use of the same profilometric technique by the crystal manufacturer ensures consistency between laboratory characterization and delivered crystal specifications.

A photograph of the AltiSurf 520 optical profilometer is shown in Fig. 1.10.

The curvature measurement procedure is based on the reconstruction of the crystal surface profile along the bending direction. The crystal is mounted on the profilometer sample holder and carefully aligned so that the longitudinal bending axis is parallel to the scanning direction of the instrument. Particular care is taken to minimize tilt and lateral misalignment, which would otherwise introduce systematic contributions unrelated to the intrinsic curvature.

Once aligned, the optical sensor measures the distance between the probe and the crystal surface while scanning along a predefined linear trajectory. At each position, the local surface height is recorded with respect to the instrument reference frame. By scanning the full crystal length, a one-dimensional surface profile $z(x)$ is obtained, where x denotes the coordinate along the bending direction.

The measured data are subsequently processed to remove rigid-body components, such

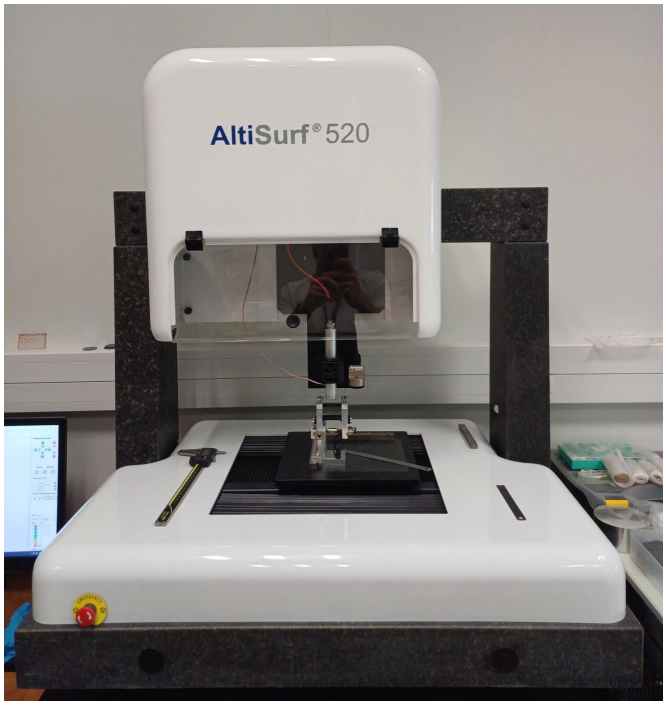

Figure 1.10: AltiSurf 520 optical surface profilometer used for the characterization of silicon crystal surfaces.

as global tilt and offset. The resulting profile is then interpolated and fitted using an analytical model, typically a circular arc in the case of uniform bending. From the fit parameters, the curvature radius R of the crystal surface is directly extracted through geometrical relations.

Although optical profilometry probes the external surface rather than the internal crystallographic planes, it provides a reliable estimate of the macroscopic curvature imposed by the bending mechanism.

2 Autocollimator-based measurement of crystal curvature

This chapter presents the autocollimator-based approach developed to measure the curvature of small bent silicon crystals. It first explains the operating principle and optical geometry of autocollimators, then describes the specific Thorlabs-based instrument and detector used in our setup. Measurement strategies for different crystal geometries (strip and RD22 types) are detailed, together with the image-acquisition and analysis steps that convert detector signals into local angles and curvature estimates.

2.1 Autocollimator structure

Autocollimators are high-precision, non-contact instruments for angular measurement. Their principal applications are calibration and measurement tasks in optical and mechanical engineering: they are used to evaluate the inclination of a surface relative to a plane perpendicular to the emitted light. Typical uses include testing parallelism of two surfaces, straightness and flatness measurements, evaluation of transparent wedges (by reference mirror), measurement of prism angles, determination of lens focal lengths, and similar tasks.

An autocollimator combines the functions of a collimator and a telescope in a single unit; the collimator and telescope share the same optical path, which is implemented using either a physical or a geometrical beam-splitting element [22]. The basic principle is to direct a collimated optical signal at a reflective surface and to derive angle information by sensing the position of the returned signal on a detector or reticle.

Figure 2.1 illustrates the case of a surface perpendicular to the autocollimator optical axis. The instrument comprises a light source and an achromatic doublet lens that collimates the light emitted by the source. Parallel rays strike the reflecting surface and

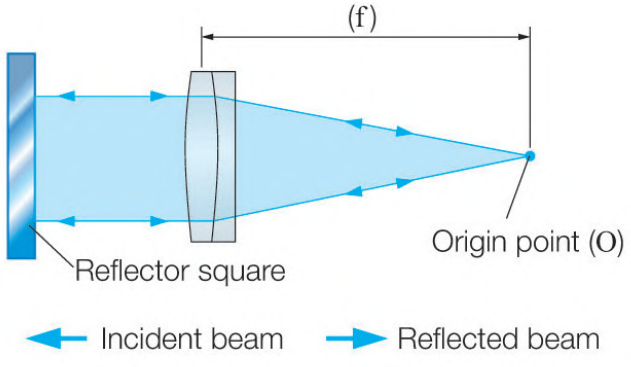

Figure 2.1: Working principle of an autocollimator with a perpendicular reflecting surface.

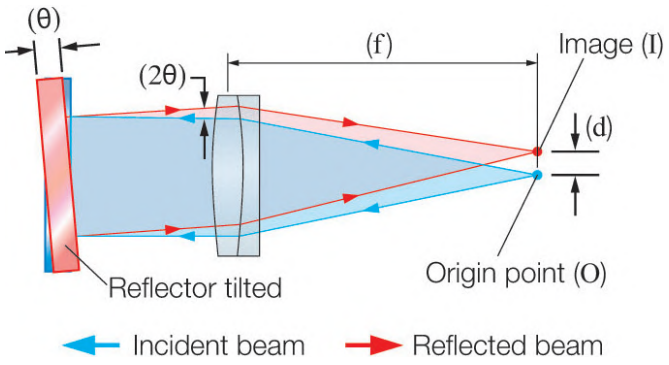

Figure 2.2: Working principle of an autocollimator with a tilted reflecting surface.

are returned through the lens to the focal plane. The distance between the light source (or reticle) and the lens is the instrument focal length.

Figure 2.2 shows the case of a slightly tilted surface. The reflected rays are displaced at the focal plane but the focal length remains the same. The displacement of the return image with respect to the optical axis can be used to determine the surface tilt. By imaging a two-dimensional pattern, the two coordinates of the reflected point are obtained: the displacement along the y-axis gives the tilt about the x-axis and the displacement along the x-axis gives the tilt about the y-axis.

It is well known that a beam reflected from a tilted mirror is deflected by twice the mirror tilt. This fact will be used below to derive the autocollimator relation between image displacement and surface tilt. First, the instrument construction must be described.

Figure 2.3 shows a common autocollimator layout: a reticle (typically a crosshair) is illuminated by a light source and placed at the lens focal plane. The lens projects the reticle pattern as a collimated beam toward the test surface; the reflected beam is

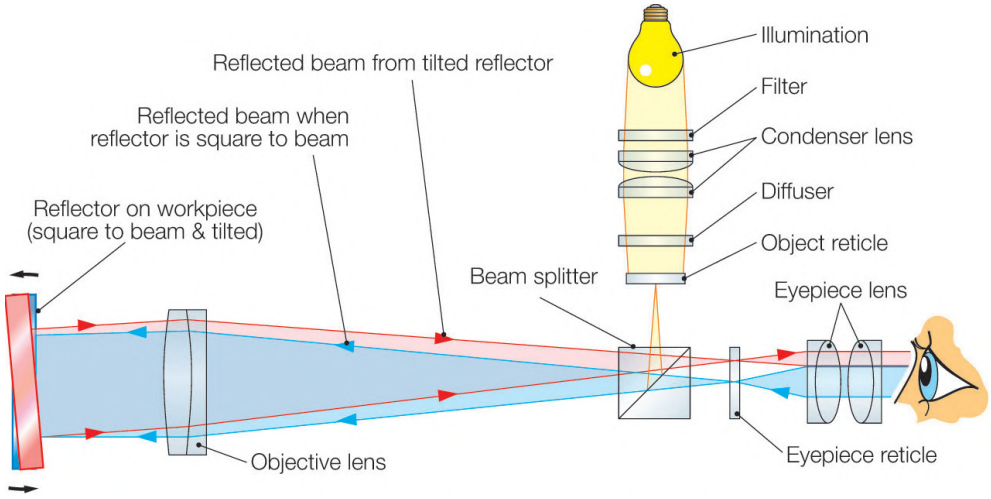

Figure 2.3: Detailed diagram of an autocollimator.

returned by the surface and refocused at the reticle plane, producing the autocollimation image.

When the reflecting surface is perpendicular to the optical axis the returned beam coincides with the emitted beam and the image matches the reticle. As shown in figure 2.4, if the mirror is tilted by an angle α, the incident beam meets the mirror at angle $\epsilon = \alpha$; after reflection, the beam returns to the objective at an angle $\sigma = 2\epsilon = 2\alpha$ relative to the optical axis. The image on the reticle plane is shifted by an amount proportional to σ; for a focal length f the transverse displacement Δy at the focal plane satisfies, for small angles,

$$\Delta y = f\,\sigma = 2f\alpha.$$

Therefore the surface tilt α can be obtained from the measured image shift as

$$\alpha = \frac{\Delta y}{2f} \tag{2.1}$$

If the autocollimator is calibrated to read angles directly, its reading $\Delta\theta_y$ equals α (because the instrument internally divides the reflected-beam angle by two) [23, 24].

2.1.1 Thorlabs instrument description

A description of the Thorlabs autocollimator used in the experiments follows. Refer to Figure 2.6 as a reference: the autocollimator shown is assembled from Thorlabs

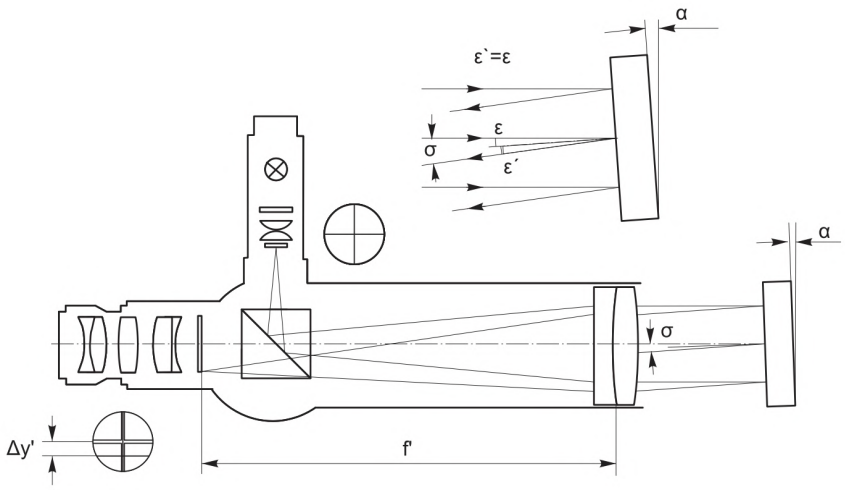

Figure 2.4: Geometry of a tilted mirror in an autocollimator measurement.

components. The main tube contains an achromatic doublet lens with focal length $f = 25\,\text{cm}$ and diameter of 50 mm. At the end of the tube there is a beam splitter (Thorlabs part `CCM1-BS013/M`) [25]; Figure 2.5 shows the component and a schematic of its operation. The beam splitter receives light from a white LED source and redirects the beam through the objective lens along the optical tube. The beam is attenuated by a 150 µm pinhole.

A laser diode can also be coupled into the beam splitter. In general the laser is avoided during curvature measurements because the iris and other apertures produce diffraction effects [26]; however, the laser is useful for alignment and calibration when the iris is removed because it provides a sharp reference point for calibrating the optical axis and detector position. A detailed description of the calibration procedure follows in the next section.

Downstream of the beam splitter, a high-precision IDS camera (model `U3-36P0XLE-M-GL`) is used. This camera features a CMOS monochrome sensor with an active array of 5136×3856 pixels (approximately 19.8 Mpx, aspect ratio 4:3), a pixel pitch of 1.4 µm, and an active area of $7.168 \times 5.376\ \text{mm}^2$. The analog-to-digital converter provides 10-bit output and supports frame rates up to 14 fps via a USB Type-C interface (USB-powered) [27].

Previously, an EO-2018 LE (UI-3250) monochrome camera was used; it provided a resolution of 1.92 Mpx with an active array of 1600×1200 pixels, a pixel size of

$4.5 \times 4.5\ \mu m^2$, and an effective sensing area of $7.2 \times 5.4\ mm^2$ [28]. The installation of the IDS camera improved the imaging resolution of the system by reducing the pixel size while maintaining approximately the same detector active area; this increases the number of pixels covering the same field of view and hence the spatial sampling of the image [29]. The impact of this upgrade on measurement precision and results is discussed in chapter 4.

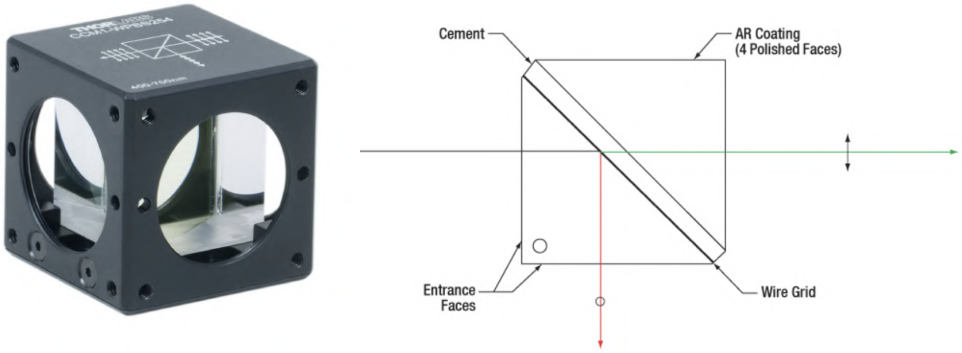

Figure 2.5: Beam splitter and scheme of functioning.

A quick estimate of the angular resolution of the autocollimator can be obtained from the relation between image displacement at the focal plane and mirror tilt. As seen, for small angles,

$$\alpha = \frac{\Delta y}{2f},$$

where Δy is the transverse shift at the focal plane and f is the focal length of the objective.

Taking $f = 25\,\text{cm} = 0.25\,\text{m}$ (the achromatic doublet used) and treating one camera pixel as the smallest resolvable displacement, the single-pixel-limited angular resolutions are:

Using the previous camera (pixel pitch $\Delta y = 4.5\,\mu\text{m}$):

$$\alpha_1 = \frac{4.5 \times 10^{-6}\ \text{m}}{2 \times 0.25\ \text{m}} = 9.0 \times 10^{-6}\ \text{rad} = 9.0\ \mu\text{rad}.$$

Using the current camera (pixel pitch $\Delta y = 1.4\,\mu\text{m}$):

$$\alpha_2 = \frac{1.4 \times 10^{-6}\ \text{m}}{2 \times 0.25\ \text{m}} = 2.8 \times 10^{-6}\ \text{rad} = 2.8\ \mu\text{rad}.$$

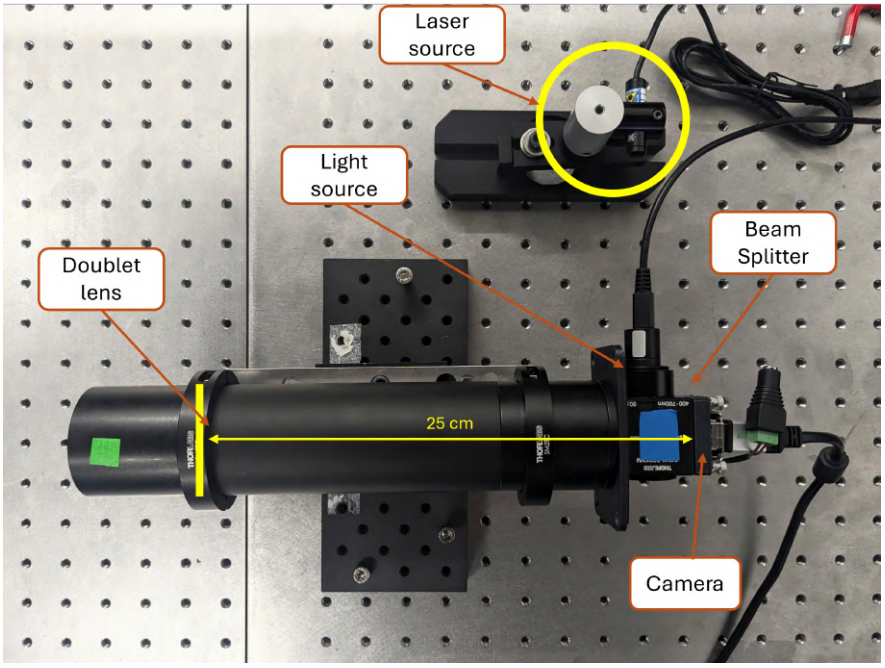

Figure 2.6: Autocollimator setup assembled from Thorlabs components, including the objective lens, beam splitter, illumination system, and CMOS camera used for curvature measurements.

Thus the current camera improves the single-pixel-limited angular resolution by a factor

$$\frac{\alpha_1}{\alpha_2} \approx \frac{4.5}{1.4} \approx 3.2.$$

Finally, it is important to note that an autocollimator effectively fixes the imaging focal plane, thanks to the detector (camera) that is located at the lens focal plane. As a consequence, all returned images formed at the focal plane share the same angular-to-transverse magnification, so a given angular tilt of the test surface produces a reproducible transverse displacement on the camera. Therefore a measured displacement on the detector always corresponds to the same angular displacement of the illuminated object (within the paraxial approximation and the instrument's field of view), which justifies using pixel shifts as a stable metric for angle and curvature measurements.

2.2 Measurement methods

The autocollimator is designed to measure the angular deviation of a plane surface (assumed locally planar) relative to the plane perpendicular to the instrument optical

axis. To measure the curvature of a non-planar surface, the instrument must be used in a non-standard way: the measured quantities become distances (in pixels) between points in the captured image rather than absolute reticle positions. Consequently, the measurement is self-referenced rather than referred to a fixed reticle mark. The returned images depend on the crystal under test: different shapes and dimensions produce different image patterns. Therefore, ad hoc measurements methods are required for each crystal type. The following paragraphs describe the methods developed for the crystals considered in this work.

2.2.1 Strip crystal

The strip crystals are the thinnest specimens used; their nominal dimensions are 70 mm × 1 mm with thickness 0.5 mm or 0.3 mm. Figure 2.7 shows a strip crystal mounted in its holder. The holder clamps the crystal at two points separated by 4 cm, and a screw at the bottom applies the bending moment. Consequently, the actual bent region is only 4 cm long; within this span both the primary curvature (along the strip length) and the anticlastic curvature (the transverse curvature arising from Poisson effects) are observed. Additionally, the small thickness of these strip crystals enhances channeling efficiency. Because the probability of dechanneling and of incoherent multiple scattering increases with the path length inside the material, a reduced thickness lowers transverse-energy diffusion and the likelihood of particles leaving the channel. Consequently, thinner strips tend to yield a higher fraction of transmitted channeled particles and better-preserved deflection angles, all else being equal.

When a strip crystal is observed with the autocollimator, the returned image typically appears rectangular, figure 2.8 shows an example. The rectangular outline corresponds to the illuminated portion of the crystal, and its projected length depends on the crystal bending: when the crystal is relaxed the rectangle length is minimal; when the crystal is curved (convex as seen by the autocollimator in the examples reported here), the reflected light is distributed over a larger angular interval and the rectangle appears longer. Figure 2.9 shows two illustrations produced with an optical simulator [30].

In principle, knowing the total arc length of the reflected footprint would suffice to

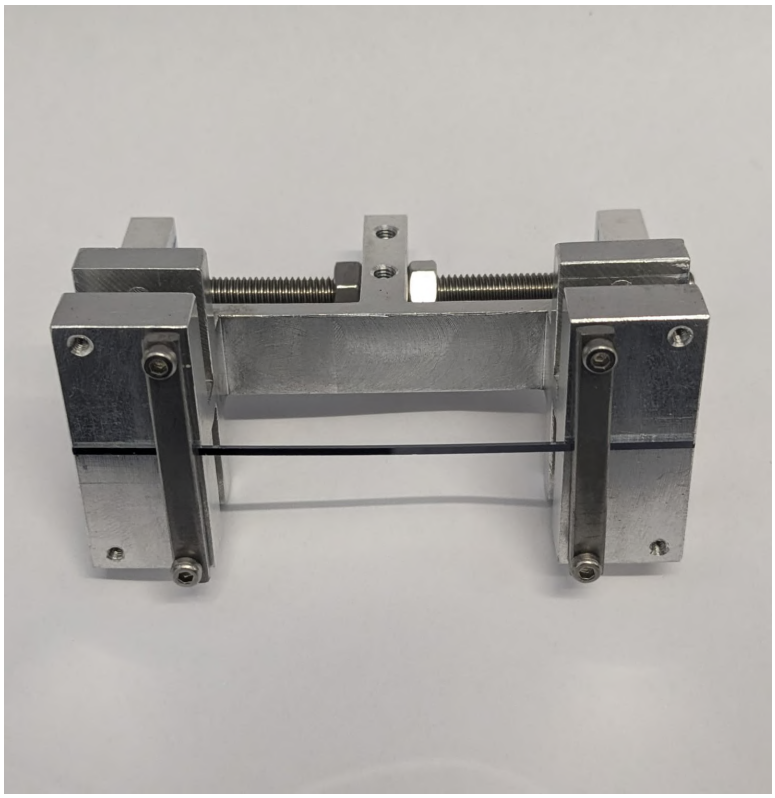

Figure 2.7: Strip crystal mounted on its holder.

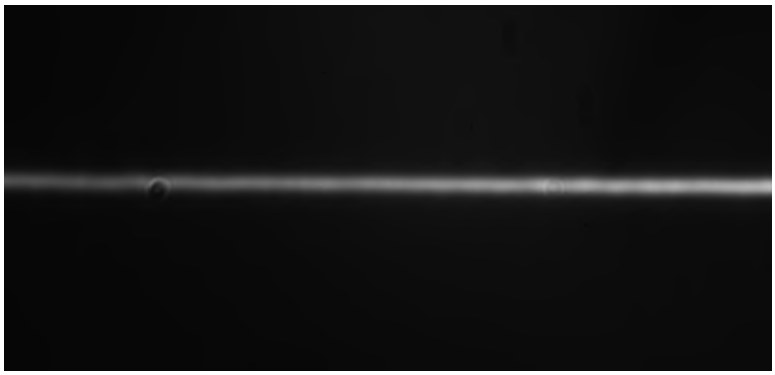

Figure 2.8: Strip crystal (0.5 mm × 1 mm × 70 mm, thickness × width × length) observed with the autocollimator. The intensity difference between the two ends of the image indicates the crystal is not perfectly centered on the detector; the left-hand side receives rays that are more obliquely incident.

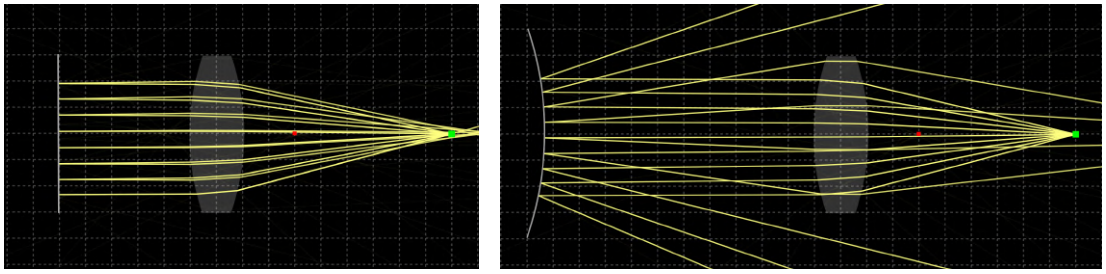

(a) Reflection from a flat surface. **(b)** Reflection from a convexly curved surface.

Figure 2.9: Reflection examples from an optical simulator: (a) relaxed strip with parallel projected rays; (b) convexly curved strip producing increased angular spread.

evaluate curvature, but the autocollimator objective and detector often do not capture the entire reflected beam; only a portion of the rectangle is visible.

To increase the robustness of the measurement, a slot is introduced in the optical path to limit the received light and produce a small rectangular footprint on the detector; figure 2.10 illustrates a photo of the 3D printed slot. The slot used has a length of 3 mm and consists of two movable blades that allow the aperture to be oriented either vertically or horizontally as required. As the crystal curvature increases, this rectangle widens. This arrangement yields more repeatable local measurements, provides additional sampling points across the crystal, and facilitates statistical analysis of the local curvature.

Primary curvature measurement procedure description

The procedure for measuring the primary curvature of the strip crystals follows these steps:

1. First, the perpendicularity of the crystal central point is calibrated. The central point is chosen as reference because, in the idealized geometry, the ray reflected from the central region returns along the optical axis and therefore exhibits minimal angular spread; this holds for both primary and anticlastic curvature measurements. For this step the autocollimator illumination is temporarily replaced by a laser source that produces a small, well-defined spot that can be located and centered on the crystal's central point. Using the Thorlabs kinematic mounts (Figure 3.5), the crystal is adjusted with respect to the plane of its front face until the reflected laser beam coincides with the incident beam, indicating

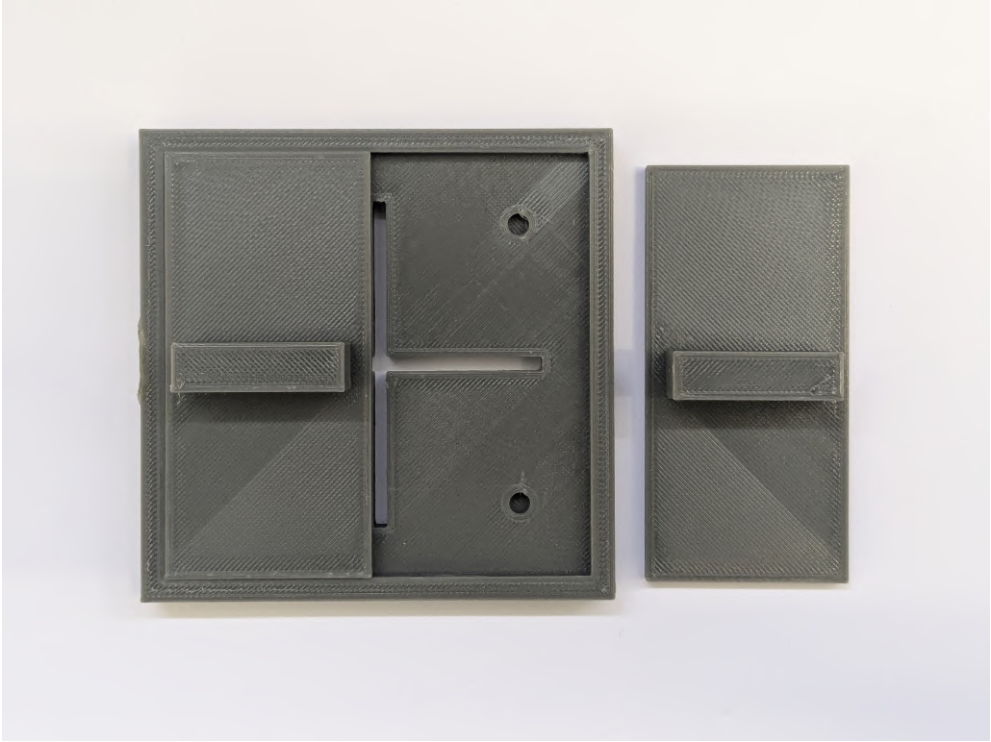

Figure 2.10: 3D printed slot to limit the recieved ligth coming into the Autocollimator.

correct alignment.

2. The slot is positioned between the autocollimator and the crystal to limit the received light and produce a well-defined rectangular footprint on the detector. The resulting rectangle is shown in Figure 2.11.

3. The central point of the rectangle is determined for each acquisition. Practically this is done by recording the two extreme edges of the illuminated rectangle and computing their midpoint (for example $y_{\text{mid}} = (y_{\text{left}} + y_{\text{right}})/2$). The crystal is then translated by a prescribed step and a new image is acquired; the rectangle shifts on the detector and the new central point is evaluated. This procedure is repeated to scan the entire accessible region of the crystal.

4. For each consecutive pair of acquisitions the differential displacement in detector pixels is computed,

$$\Delta y_{\text{px}} = y_{\text{mid},\,i+1} - y_{\text{mid},\,i}.$$

The pixel displacement is converted to a physical length using the camera pixel

pitch p_{px} (from the camera datasheet or an experimental calibration),

$$\Delta y = \Delta y_{\text{px}} \times p_{\text{px}} \quad \text{(meters)}.$$

This Δy is the quantity that enters the autocollimator relation to obtain the local angular change:

$$\theta \approx \frac{\Delta y}{2f}, \tag{2.2}$$

where f is the objective focal length. Using consecutive differences makes the measurement self-referenced: the first point serves as a reference and the relative displacement Δy indicates how much the reflected image moves when the crystal is stepped by a known mechanical increment, independently of the absolute initial reflection angle.

5. Finally, the radius of curvature is obtained using the small-angle approximation. For a circular arc of radius R and subtended angle θ the arc length is

$$\ell = R\,\theta.$$

If θ is small the arc length ℓ is well approximated by the chord length (the mechanical step) s, hence

$$R \approx \frac{s}{\theta}.$$

Combining with equation (2.2) gives the working formula used in the analysis:

$$R \;\approx\; \frac{s}{\theta} \;=\; \frac{s}{\Delta y/(2f)} \;=\; \frac{2f\,s}{\Delta y},$$

where s and Δy must be expressed in metres and θ in radians.

6. Propagate uncertainties from the mechanical step s, pixel measurement Δy_{px}, and focal length f to obtain the uncertainty on R. For small relative errors,

$$\frac{\delta R}{R} \approx \sqrt{\left(\frac{\delta s}{s}\right)^2 + \left(\frac{\delta(\Delta y)}{\Delta y}\right)^2 + \left(\frac{\delta f}{f}\right)^2}.$$

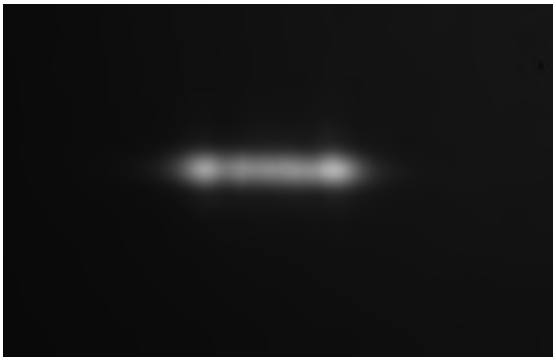

Figure 2.11: Partial illumination observed with the autocollimator when a slot is placed between the autocollimator and the strip crystal.

Anticlastic curvature measurement procedure

The measurement of the secondary (anticlastic) curvature requires a different approach with respect to the primary curvature. Due to the small width of the crystal strip, the slot-based method adopted for the primary curvature cannot be applied. For this reason, a geometry-based method exploiting a self-referenced flat region of the crystal is employed.

As shown in Fig. 2.13, the light reflected by the anticlastic deformation is entirely collected by the detector. Therefore, the curvature information is encoded in the vertical extension of the reflected image. For small angular deviations, the spatial angle subtended by the reflected beam corresponds directly to the angular variation of the surface normal induced by the anticlastic curvature.

A key aspect of the method is that the same angular spread on the detector may result either from a larger curvature acting over a short surface or from a smaller curvature acting over a longer surface. Consequently, the effective illuminated length of the crystal must be taken into account in order to correctly relate the detected image height to the curvature angle.

Figure 2.12 shows a photograph of the flat surface of the strip crystal while figure 2.13 illustrates a simplified geometrical scheme of the measurement principle. The vertical axis represents the detector plane, while the yellow horizontal lines indicate the reflected light, implying that the incoming light rays are always parallel to each other and perpendicular to the flat surface. The straight blue segment corresponds to a flat

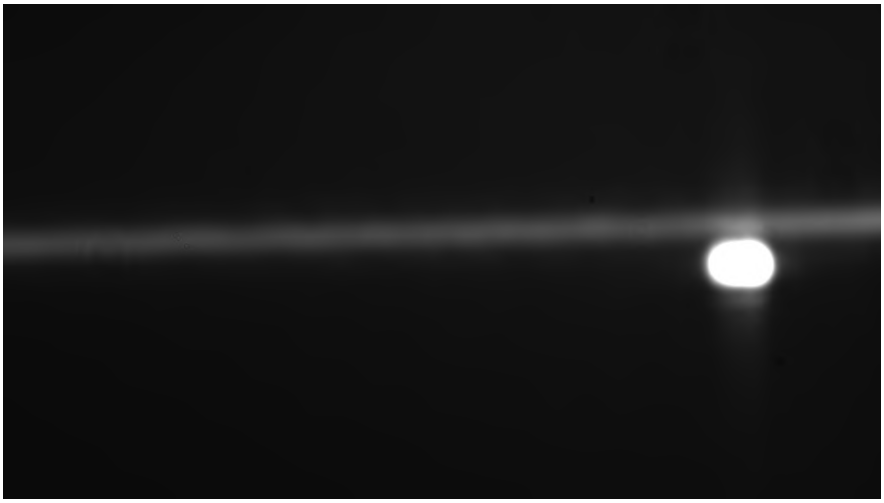

Figure 2.12: Strip crystal flat surface seen on Autocollimator.

reference region of the crystal, whereas the curved blue profile represents the anticlastic deformation. For clarity, the optical magnification of the imaging system is neglected and the crystal dimensions are rescaled to emphasize the geometrical relations.

Thanks to the holder geometry, a small flat portion of the crystal remains accessible even when the strip is bent. When this flat region is illuminated by the autocollimator, the reflected rays return without angular deviation, producing an image on the detector whose vertical extension Δp_{tot} corresponds to the full illuminated length of the surface, scaled by the camera magnification. This quantity is determined experimentally and serves as a zero-curvature reference.

When the anticlastic curvature is present, the local tilt of the surface causes an angular spread of the reflected rays. As a consequence, only a smaller portion of the detector is illuminated, with a vertical extension denoted as Δp_c, as illustrated in Fig. 2.13. The difference between the flat and curved configurations defines the displacement

$$\Delta y = \Delta y_{\text{tot}} - \Delta y_c, \tag{2.3}$$

where Δy_{tot} and Δy_c are obtained by converting the corresponding pixel values into physical units.

From a geometrical point of view, considering half of the illuminated region is sufficient. As shown in the right panel of Fig. 2.13, the quantity $\Delta p_c/2$ corresponds to the

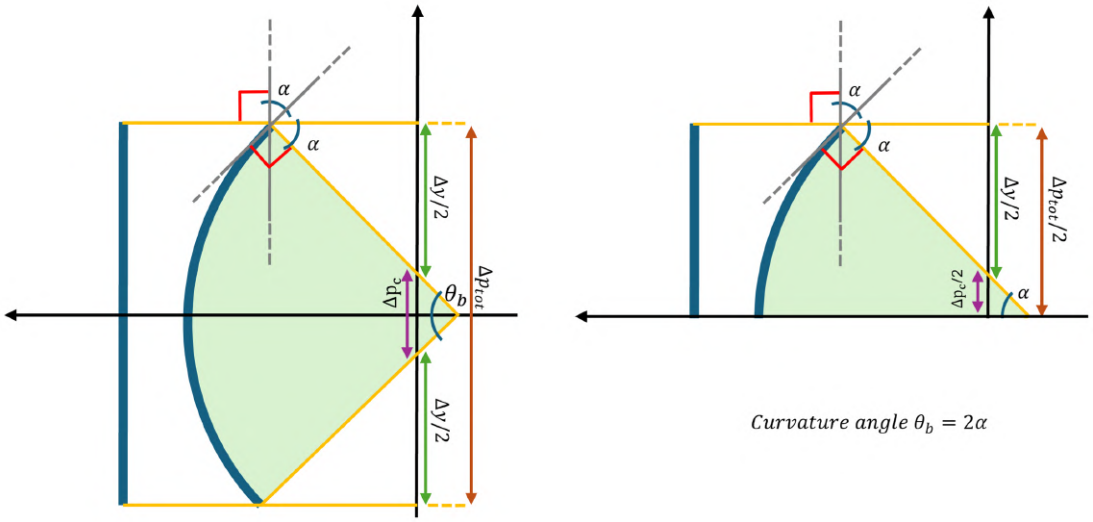

Figure 2.13: Geometrical scheme for the measurement of the anticlastic curvature

displacement produced on the detector by a surface tilt angle α. Due to the symmetry of the anticlastic deformation, the total curvature angle θ_b is given by

$$\theta_b = 2\alpha. \tag{2.4}$$

Therefore, once Δy is measured, the anticlastic curvature angle can be directly evaluated using the autocollimator relation introduced in Eq. 2.2.

The associated standard uncertainty is evaluated by propagating the uncertainty on Δy through the autocollimator calibration. Assuming a linear response of the instrument in the small-angle regime, the uncertainty on θ_b can be written as

$$u(\theta_b) = \left|\frac{\partial \theta_b}{\partial \Delta y}\right| u(\Delta y), \tag{2.5}$$

where the sensitivity $\partial\theta_b/\partial\Delta y$ is determined by the autocollimator optical parameters defined in the previous sections.

The quantity Δy is defined as the difference between the image height measured in the flat reference configuration and that obtained in the presence of anticlastic curvature,

$$\Delta y = \Delta y_{\text{tot}} - \Delta y_c. \tag{2.6}$$

Assuming uncorrelated contributions, its uncertainty is given by

$$u(\Delta y) = \sqrt{u^2(\Delta y_{\text{tot}}) + u^2(\Delta y_c)}. \tag{2.7}$$

Both Δy_{tot} and Δy_c are obtained from pixel measurements, so that the dominant contributions to the uncertainty arise from the determination of the image height on the detector and from the calibration of the pixel-to-meter conversion factor. Additional statistical contributions due to measurement repeatability are estimated from repeated acquisitions and summed in quadrature.

2.2.2 RD22 crystal

The RD22 crystals were originally developed in the early 1990s within the framework of the CERN RD22 collaboration, whose goal was to investigate the feasibility of proton beam extraction from high-energy storage rings using bent silicon monocrystals [31].

The RD22 project represented one of the first systematic experimental efforts to study bent-crystal channeling in conditions relevant for accelerator operation. Beyond the immediate objective of extracting a fraction of the circulating beam, the collaboration explored the implications of crystal curvature, crystal geometry, and mechanical bending schemes on channeling efficiency and angular acceptance [32].

From a structural point of view, the RD22 crystals consist of *"C-shaped"* silicon monocrystals with millimetric transverse dimensions and a length of a few centimeters along the beam direction, a photo and geometrical dimensions are shown in 2.14. Unlike the thin strip crystals discussed in the previous sections, RD22 crystals are relatively thick and mechanically stiff. They are typically bent by clamping their extremities onto specifically designed holders, producing both primary curvature and anticlastic one.

The measurement of the anticlastic curvature of the RD22 crystals is performed using the same zero-reference method previously introduced for the anticlastic curvature of strip crystals. Since the method has already been discussed in detail, only a brief description is provided here, focusing on the specific features of the RD22 geometry and on the physical interpretation of the measured signal.

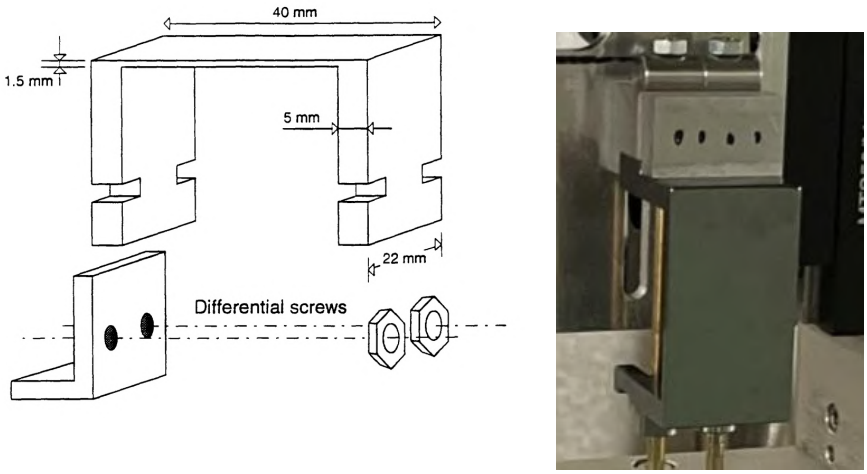

Figure 2.14: RD22 crystal. (a) *C-shaped* crystal drawing with geometrical dimensions [32]. (b) Photograph of the RD22 crystal mounted on a goniometer in the H8 North Area before the test beam.

For RD22 crystals, the anticlastic curvature plays a central role, as it corresponds to the curvature responsible for the deflection of the particle beam. In fact, the beam crosses the crystal along the short dimension (22 mm), which is intentionally chosen to reduce dechanneling effects. However, despite this favorable geometry, the transverse width of RD22 crystals is significantly larger than that of strip crystals, resulting in a lower expected channeling efficiency.

Due to the mechanical design of the crystal holder, the RD22 crystal exhibits a characteristic curvature profile. The upper and lower borders of the crystal are mechanically connected to flat supporting legs, which enforce local flatness at the extremities. As a consequence, the anticlastic curvature is maximum at the center of the crystal and gradually decreases towards the borders, where it can be considered effectively zero.

This behavior is clearly reflected in the autocollimator image of a bent RD22 crystal, shown in Fig. 2.15. The reflected light footprint exhibits an hourglass-like shape: the upper and lower flat regions reflect light rays perpendicular to the surface, producing wider illuminated areas on the detector, while the central region, where the anticlastic curvature is present along the horizontal direction, causes the reflected rays to converge inward, resulting in a narrower image width. It is important to note that the reflected rays do not converge before reaching the detector plane, as the radius of curvature is

much larger than the distance between the crystal and the camera.

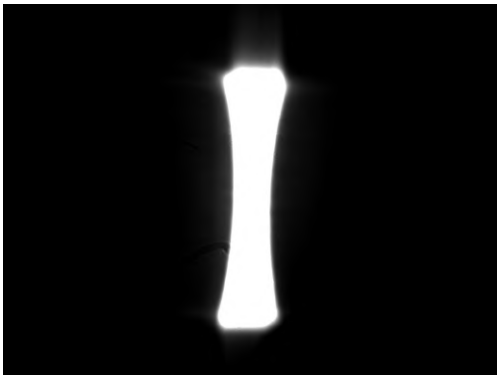

Figure 2.15: RD22 crystal observed with the autocollimator. The crystal is slightly bent and the full reflected light is collected by the camera in this configuration.

The measurement procedure consists in comparing the width of the reflected image corresponding to the flat reference regions with that measured at the center of the crystal, where the anticlastic curvature is maximum. The displacement between these two configurations provides the quantity needed to directly evaluate the curvature angle through the autocollimator relation. The same geometrical considerations discussed for strip crystals apply, and the simplified scheme shown in Fig. 2.13 can be used as a reference for the interpretation of the measurement.

Finally, an additional analysis made possible by the RD22 geometry consists in performing multiple measurements of the reflected image width at different vertical positions along the crystal. This allows the reconstruction of the curvature gradient from the upper to the lower edge of the crystal. A detailed discussion of this multi-point curvature analysis is deferred to the final chapter, where the experimental results are presented and discussed.

3 Measurement automatization

This chapter describes the automation of the measurement system: the motion hardware, the controller firmware and the software used to acquire and process high-resolution images. Requirements and system architecture are presented, followed by details on the motorized XY stages, mechanical mounts, the non-blocking Arduino firmware for precise positioning and homing, and the Python image-processing pipeline. Key analysis methods (PCA, Savitzky–Golay filtering) and the specific algorithms implemented for RD22 and strip crystals are also outlined.

3.1 Project overview and requirements

The automation of the measurement system described in the previous chapter is necessary for several reasons: **measurement repeatability**, **user independence**, and **time savings**. The automation consists of automatic movement of the crystal and automatic image recognition, enabling the final value to be obtained without user-dependent calculations.

Repeatability is improved by automatic movement. Using a biaxial *XY* translation stage, it is possible to return the crystal to the same position with greater accuracy than with a manual stage, reduce the nominal step, and provide more linear stroke allowing the scan of long crystals. As shown in the previous chapter, the manual translation stage had a nominal step of 10 µm but was strongly dependent on user skill and affected by reading errors such as parallax. The automatic stage improves both the accuracy and the repeatability of positioning. In addition, other errors in the manual system arise from manual image recognition. An image-recognition algorithm makes the measurements independent of the user and more repeatable. Finally, the automated process greatly reduces the time required for a measurement: the previous procedure

took several hours, whereas the automated system can complete it in a few minutes.

Requirements

The system shall comply with the following requirements to ensure full scanning of the crystal and adequate spatial resolution in the curvature mapping:

1. Motion stage: stable, repeatable step movements with **resolution and repeatability** $\leq 100\,\mu m$**; total travel: 100 × 100 mm²**.
2. Image capture: software capable of interfacing with **IDS U3-series cameras** and acquiring images at the camera's full frame rate and bit depth (10-bit, up to 14 fps for the U3-36P0XLE-M-GL).
3. Image processing: automated routines able to handle high-resolution images up to **5136 × 3856 pixels**, including ROI extraction, edge detection, centroiding and subpixel interpolation.
4. **Data analysis and statistics**: automated calculation of summary statistics (mean, standard deviation, confidence intervals) on repeated measurements to quantify measurement uncertainty; support for exporting results and metadata (timestamp, stage position, camera settings, acquisition parameters).

To provide a clearer project overview, the following steps were implemented to realize the automated system:

- Automatic translation stages using stepper motors controlled by a microcontroller
- Design and fabrication of mechanical support brackets
- Python-based image processing to extract data

The figure 3.1 shows a block diagram of the overall system.

3.2 Automatic translation stages

The automatic translation stages are implemented using two NEMA 23 stepper motors and two linear actuators with lead screws. Based on laboratory availability, the horizontal stage was sourced from a UA9 stage system that had been used previously

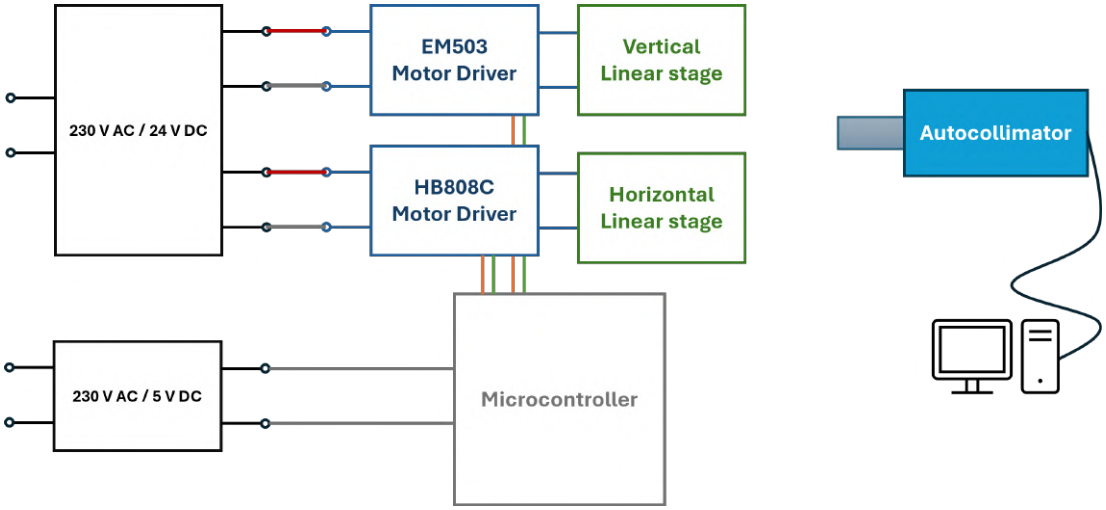

Figure 3.1: Block Diagram of the overall system

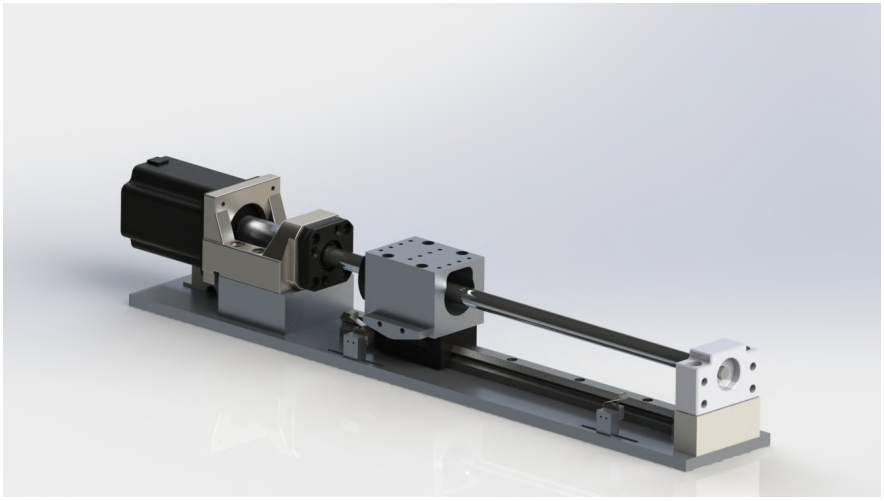

Figure 3.2: 3D drawing of the horizontal stage made in SolidWorks 3D CAD [33].

for different purposes and is currently unused. This stage was previously employed for plastic-scintillator detector placement in a high-energy particle beam [33]. The stage, shown in Figure 3.2, has a screw pitch of 4 mm, a total stroke of approximately 200 mm, a thrust exceeding 10 kg, repeatability better than 10 µm, and a maximum speed of 10 mm s^{-1} with a resolution of 1 µm when using 20× microstepping. Repeatability is ensured by the stepper motor, which has 200 steps per revolution (i.e., 1.8° per step) [34]; microstepping implemented by the driver increases this to 4000 steps per revolution. Microstepping improves repeatability and enables precise crystal scanning with very fine movements.

The motor for the linear stage is connected in the bipolar configuration. The differences

between bipolar and unipolar configurations lie in the way the motor windings are driven: in the unipolar configuration a center tap on each phase is connected to the motor supply so that commutation is achieved by switching sections of the windings. In this case current flows in only one direction per winding section and the drive circuitry can be simpler. In the bipolar configuration, because there are no center taps, the windings must be driven with current flowing in both directions; the driver therefore requires H-bridge style electronics to reverse the current. The bipolar configuration provides higher torque because it energizes the full winding (though with higher inductance), but this typically reduces maximum speed compared to an equivalent unipolar drive. This behavior follows the inverse-proportional relationship of output torque with motor speed and inductance:

$$\tau \propto \frac{V_m}{v\sqrt{L}}, \tag{3.1}$$

where τ is the torque, V_m is the motor supply voltage, v is the motor speed, and L is the motor inductance.

To drive the motor, an EM503 motor driver is used according to lab availability. The EM503 is a two-phase digital stepper drive capable of accepting 20–50 V input and of providing a driving current from 0.21 to 3 A. It implements sensorless stall detection that allows detection of motor stall or loss of steps without the use of external position sensors. The method is based on real-time monitoring of the motor electrical behavior: when the rotor is unable to follow the commanded motion, abnormal variations in current and back electromotive force are detected by the DSP, triggering a fault condition. The maximum pulse input frequency is 200 kHz. Figure 3.3 illustrates the connections.

The digital input signals are PUL+ and PUL- (pulse signal). In single-pulse mode, each active edge (rising or falling, software-configurable) activates a step. In double-pulse mode (software-configurable) the input represents clockwise pulses, active on both high and low levels. The input accepts 4–5 V for PUL-HIGH and 0–0.5 V for PUL-LOW. For a reliable motor response, the pulse width must be longer than 10 µs, corresponding to a maximum step frequency of 100 kHz. However, a significant limitation arises from the use of the `digitalWrite()` function, which requires approximately 100 CPU cycles per call. Considering the total overhead of the motor control routine `run()`,

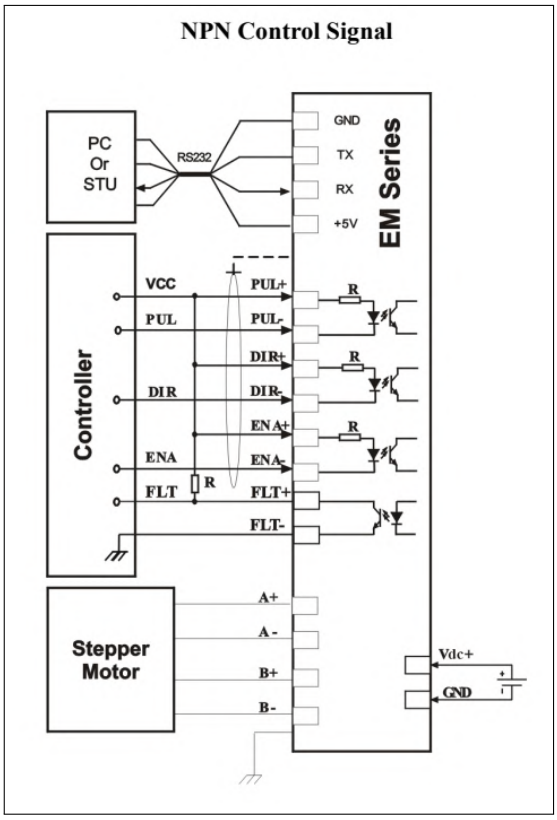

Figure 3.3: Digital stepper drive EM503 connection scheme [35].

which accounts for about 300 additional CPU cycles, each step requires roughly 400 CPU cycles.

Given the Arduino clock frequency of 16 MHz, the maximum achievable step frequency is therefore limited to

$$f_{\max} = \frac{16\,\text{MHz}}{400} \approx 40\,\text{kHz}.$$

When two motors are driven simultaneously, this frequency must be divided by two, as each motor can be serviced only once per loop iteration. Moreover, since each motor step requires both a rising and a falling edge, the effective frequency is further halved, yielding

$$f_{\max} \approx 10\,\text{kHz}.$$

Finally, introducing a conservative safety margin, the maximum operating step frequency is set to

$$f_{\max} = 8\,\text{kHz}.$$

DIR+ / DIR- are the direction signals: in single-pulse mode this input uses low/high levels to represent the two rotation directions; in double-pulse mode (software-configurable) this input represents counter-clockwise pulses, active on both high and low levels. For reliable motion response, DIR should be asserted at least 5 µs before the PUL signal. ENA+ / ENA- are the enable signals used for enabling/disabling the driver; by default a high level (NPN control) enables the driver and a low level disables it. Finally, FLT+ / FLT- are the fault/alarm outputs (open-collector), asserted when one of the following protections is triggered: over-voltage, over-current, short circuit, or stall error.

The power and motor connector pins 1 to 6 connect motor phase A+/A- and B+/B- (pins 1–4), while pins 5 and 6 are dedicated to the power supply.

All connections are made using a DB9 connector and an Arduino UNO is used for the connection, with a dedicated firmware described in the next section, finally, an overall pinout configuration is illustrated in the figure 3.8 at the end of this section.

3.2.1 Mechanical support brackets

To keep both stages together, mechanical support brackets are required. The support brackets were designed using parametric CAD modeling in *Autodesk Fusion 360*. The goal of these brackets is to secure the first stage to the second, creating a two-axis motion stage. Accordingly, an L-shaped bracket was designed; Figure 3.4 illustrates it.

Additional brackets were necessary to secure the crystal holder to the stages. These brackets provide a stable mount for the two-axis kinematic motion stage, as illustrated in Figure 3.5.

The Fusion 360 design of the crystal support brackets is shown in Figure 3.6, while a photograph of the complete assembled system is shown in Figure 3.7. The bracket is shaped to allow easy use of the left-hand kinematic mounts, creating a distance between the vertical stage and the rotating adjusters. All brackets were fabricated at the mechanical workshop of INFN in Rome.

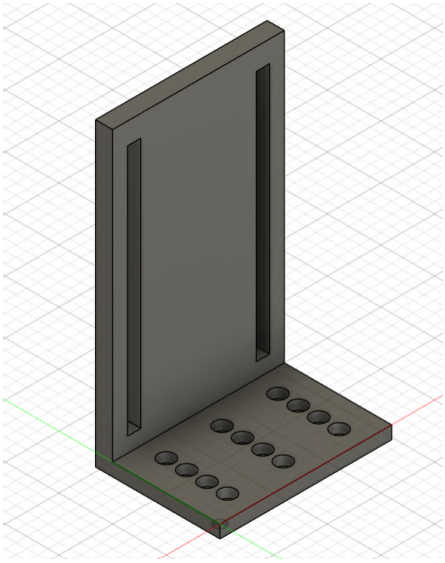

Figure 3.4: Mechanical L-shaped bracket designed in Fusion 360.

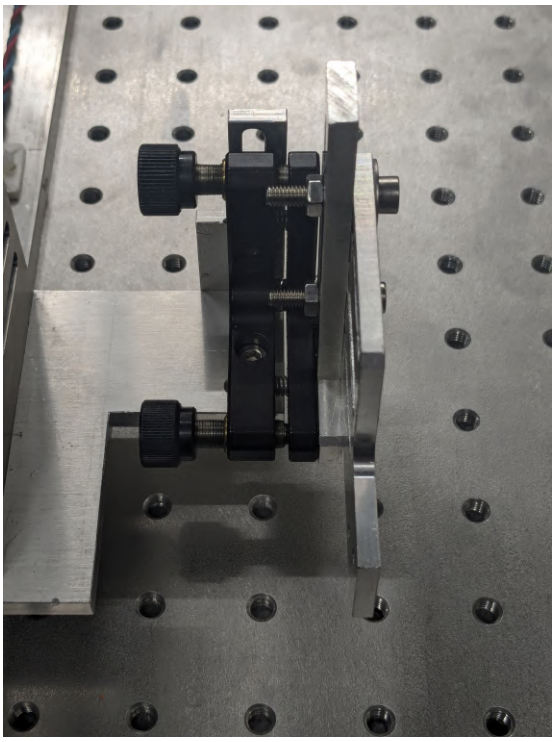

Figure 3.5: Thorlabs kinematic mounts.

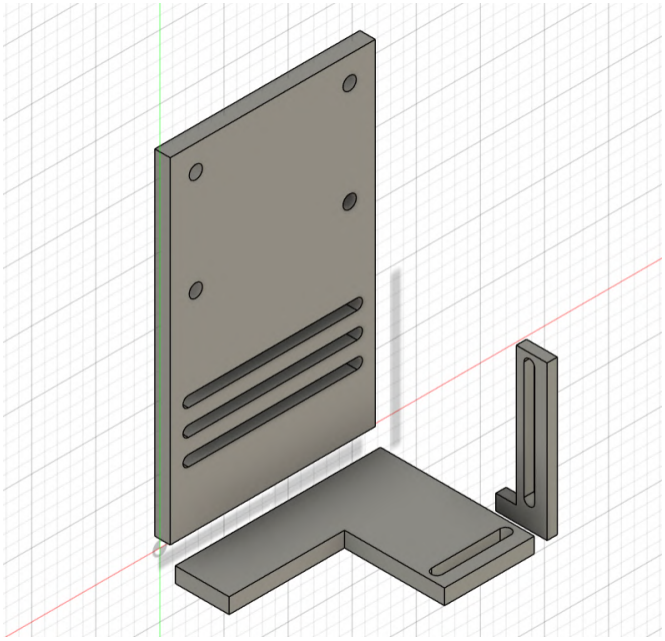

Figure 3.6: Mechanical crystal support bracket designed in Fusion 360.

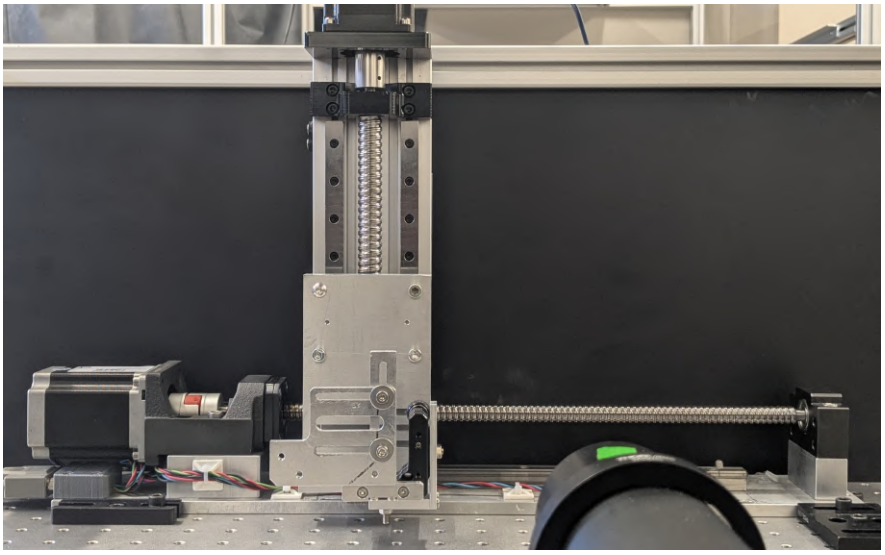

Figure 3.7: Motorized motion system: two linear stages mounted using aluminum support brackets, with additional brackets for crystal mounting.

3.2.2 XY stage controller firmware

The firmware implements a real-time, non-blocking control system for a two-axis motorized stage equipped with stepper motors and mechanical limit switches. The system supports independent motion control on the X and Y axes with distinct operational characteristics: the X axis employs a two-stage fast-homing algorithm that leverages mechanical limit switches for absolute position recovery, while the Y axis operates without limit-switch feedback and relies on manual user-defined homing. The firmware prioritizes responsive command handling, robust debouncing, safety interlock logic, and unit conversions between motor steps and physical millimeters.

Hardware architecture and pin configuration

The stage control system uses an Arduino microcontroller interfaced with two stepper motor drivers and mechanical switches. The X-axis motor is driven through digital pins for step and direction signals (`STEP_X = 7`, `DIR_X = 2`), with an enable line (`ENA_X = 6`) to control driver power. Two normally-open limit switches, `SW31` and `SW32`, are connected to analog inputs `A5` and `A0` respectively, with internal pull-up resistors enabled to provide stable high logic levels in the quiescent state. `SW31` marks the left boundary (minimum position), while `SW32` marks the right boundary (maximum position). The Y axis uses `STEP_Y = 8`, `DIR_Y = 9`, and `ENA_Y = 4`, but lacks associated limit switches, reflecting an open-loop positioning architecture. All stepper control uses the `AccelStepper` library, which abstracts the step-and-direction protocol and provides trapezoidal acceleration profiles for smooth, bounded motion.

Both axes employ lead-screw driven mechanisms with microstepping drivers to achieve fine positional resolution. The X axis is configured with a lead-screw pitch of 4.0 mm/rev and a microstepping setting that yields $N_X = 4000$ steps per revolution, corresponding to a resolution of 1 µm per step. The Y axis has a pitch of 5.0 mm/rev and $N_Y = 5000$ steps per revolution, also yielding 1 µm per step. These resolutions enable precise positioning suitable for optical alignment.

Unit conversion between motor steps and millimeters is implemented through per-axis

scaling functions. For the X axis, the forward conversion (millimeters to steps) is

$$s_X = m_X \times \frac{N_X}{P_X},$$

where m_X is the displacement in millimeters, $N_X = 4000$ is the steps per revolution, and $P_X = 4.0\,\text{mm/rev}$ is the screw pitch. For the Y axis the same scaling factor applies, but a sign inversion is incorporated to align the user-facing coordinate system with intuitive motion: positive millimeter values command upward motion while the internal stepper coordinate system may employ opposite conventions. Specifically, all Y-axis moves are internally negated before being sent to the stepper object, ensuring that a user command `MoveMMY 10` raises the stage by 10 mm.

Debouncing strategy for limit switches

Mechanical switches exhibit contact bounce: rapid electrical fluctuations when transitioning between open and closed states, that can cause spurious position limits or trigger erroneous safety interlocks. To suppress this noise, the firmware implements a non-blocking debouncer for both X-axis limit switches. Each switch is represented by a `Debouncer` structure containing the associated pin, the raw digital reading, a debounced state, a timestamp of the last raw-state change, and a debounce window duration (set to 15 ms, typical for mechanical switches). The update function compares the raw digital read to the last recorded value; if a change is detected, the timestamp is recorded. If the raw value remains stable for at least the debounce window duration, the debounced state is updated. This approach operates non-blocking within the main loop and provides robust noise suppression. The debounced switch states are used for all safety checks and homing logic, ensuring reliable detection of actual mechanical events.

Motion control and acceleration profiles

The firmware manages motor acceleration and velocity using the `AccelStepper` library, which implements trapezoidal velocity profiles. Each axis is configured with a maximum speed (default 1000 steps/s for normal moves) and acceleration (default

200 steps/s^2). These parameters define the velocity profile shape: the motor accelerates at the specified acceleration until reaching the target speed or until deceleration is required to reach the target position smoothly. The library handles step-pulse generation and direction control, requiring only calls to `moveTo()` to define targets and `run()` to execute one iteration of the motion algorithm.

Speeds and accelerations are reconfigured dynamically for different operational modes. Normal point-to-point moves use the default parameters. Homing operations use specialized fast-approach and slow-precision phases (described below). Full-length measurement uses intermediate speeds and accelerations optimized for accurate switch detection. The firmware also enforces a minimum pulse width of 10 µs to ensure driver compatibility.

The X-axis **homing** procedure rapidly locates the mechanical left limit (`SW31`) and establishes an absolute zero position despite uncertainty in the current stage position. The algorithm proceeds in two stages to balance speed and precision:

- **Stage 1**, fast approach. The homing command calculates a travel distance large enough to exceed the maximum possible stage extent, ensuring the motor encounters the left endstop regardless of starting position. The calculation is

$$\text{distance} = \left\lfloor \frac{L_{\text{total}}}{P_X} \times N_X \right\rfloor + S_{\text{margin}},$$

  where $L_{\text{total}} = 200\,\text{mm}$ is the known total travel range, $P_X = 4.0\,\text{mm/rev}$, $N_X = 4000$ steps/rev, and $S_{\text{margin}} = 15000$ steps provides a safety buffer. For the nominal configuration this yields approximately 215000 steps of target travel. The stepper is configured with a maximum speed of 7000 steps/s and acceleration of 3000 steps/s^2 to provide rapid approach while maintaining controlled dynamics. The firmware enters a `homingX` state and sets `homingStepX = 1` for this phase. In each main-loop iteration the debounced switch state is checked; when `SW31` transitions to the closed state, motion is halted.

- **Stage 2**, slow precision to release. Upon switch contact, the stepper speed is reduced to 400 steps/s with acceleration 100 steps/s^2. The motor is commanded to move forward (away from the switch) by 10000 steps at this reduced speed,

allowing switch contacts to separate and settle. The firmware sets `homingStepX = 2`. Subsequent iterations monitor the debounced switch; once `SW31` returns to the open state, the motor is stopped and the current position is set to zero via `setCurrentPosition(0)`, establishing the left endstop as the mechanical origin. Speeds and accelerations are restored to normal-motion values and the `homedX` flag is set to `true`.

This two-stage approach provides rapid coarse positioning followed by precision release, completing the homing sequence in a few seconds while preserving repeatability and avoiding damage from high-speed impacts.

The Y axis lacks mechanical limit switches and cannot guarantee absolute position recovery from hardware alone. Instead, the firmware provides a manual homing procedure: the operator places the stage at the desired Y-axis home position and issues the `HomeY` command. This command sets the stepper's current position to zero, redefining the coordinate-system origin. All subsequent Y-axis moves are then relative to this user-established home. While less robust than hardware homing, this approach is practical for stages without limit switches and places the responsibility for safe positioning on the operator.

Finally, The firmware implements protective mechanisms to prevent damage from unexpected switch triggers or command errors. During normal operation (when not homing or measuring), debounced switch states are continuously monitored. If the X axis is moving leftward (negative velocity) and the left switch `SW31` closes, an immediate motor stop is executed, the internal position is frozen, and a diagnostic message is printed. Similarly, rightward motion with a closed `SW32` triggers the same protective stop. These interlocks prevent the stage from driving into mechanical hard stops at high velocity.

Before accepting a move command, the firmware checks whether the target position would violate an active limit switch. If the left switch is asserted and a leftward move is requested, or if the right switch is asserted and a rightward move is requested, the move is rejected with an explanatory error message. All safety-related terminations call `safetyStopAll()`, which stops both motors, freezes their current positions, and

clears motion-in-progress flags.

Command interface and parsing

The firmware provides a serial command interface operating at 9600 baud, accepting ASCII commands terminated by newline characters. Commands are read non-blocking via `Serial.available()` and parsed character-by-character. Supported commands include:

- `Enable` / `Disable`: energize or de-energize the stepper drivers.
- `Stop`: immediately halt both motors.
- `MoveX <steps>`: move the X axis to an absolute step position.
- `MoveY <steps>`: move the Y axis to an absolute step position (with sign inversion applied internally).
- `MoveMMX <mm>`: move X to an absolute position in millimeters (converted to steps).
- `MoveMMY <mm>`: move Y to an absolute position in millimeters (with sign inversion).
- `Home`: execute the two-stage fast homing procedure for the X axis.
- `HomeY`: set the current Y position as the origin (manual homing).
- `CurrentPosition`: report current positions of both axes in steps and millimeters.
- `FullLength`: measure and report the total usable travel distance of the X axis.
- `ReadSW31` / `ReadSW32`: debug commands to inspect raw and debounced switch states.

Each command is processed by a dedicated branch in `parseCommand()`. Numeric arguments are extracted and converted to integers or floats as appropriate. Move commands validate bounds and switch states before updating stepper targets; homing and measurement commands initialize multi-phase state machines that execute across multiple loop iterations.

The main firmware loop executes continuously without blocking delays, employing a state-machine paradigm for multi-step operations (homing, full-length measurement) and immediate-return functions for single-step tasks (move commands, status queries). Each iteration performs the following sequence:

1. Update debouncers for both X-axis limit switches.
2. Perform safety checks (if not homing or measuring).
3. Execute homing state machine if homing is active.
4. Call `run()` on active steppers to generate step-pulse iterations.
5. Check serial input and parse commands if available.

This architecture ensures motor control remains responsive, switch monitoring is continuous, and commands are processed with minimal latency. Blocking operations are avoided; long moves are executed across many loop iterations while the loop continues to monitor switches and respond to new commands.

On power-up, `setup()` initializes hardware resources. Pin modes are configured for inputs (switch pins with pull-ups) and outputs (enable and step/direction pins). Debouncers are instantiated with their pins and debounce window. Stepper objects are configured with default speed and acceleration, current positions are initialized, and pulse-width constraints are applied. Both driver enable lines are set to the disabled state, the operator must issue `Enable` to begin motion.

The firmware is robust against commands arriving at arbitrary times: the non-blocking architecture ensures limit-switch monitoring and safety interlocks remain active. Homing may be performed as needed; boolean flags (`homedX`, `homedY`) track homing status so higher-level control software can enforce preconditions (for example requiring X homing before full-length measurement).

3.3 Image processing software

A general description of the software architecture is provided in the following. The software is organized according to *separation of concerns* and modularization. Clear separation of concerns is motivated by the need to decompose systems into smaller,

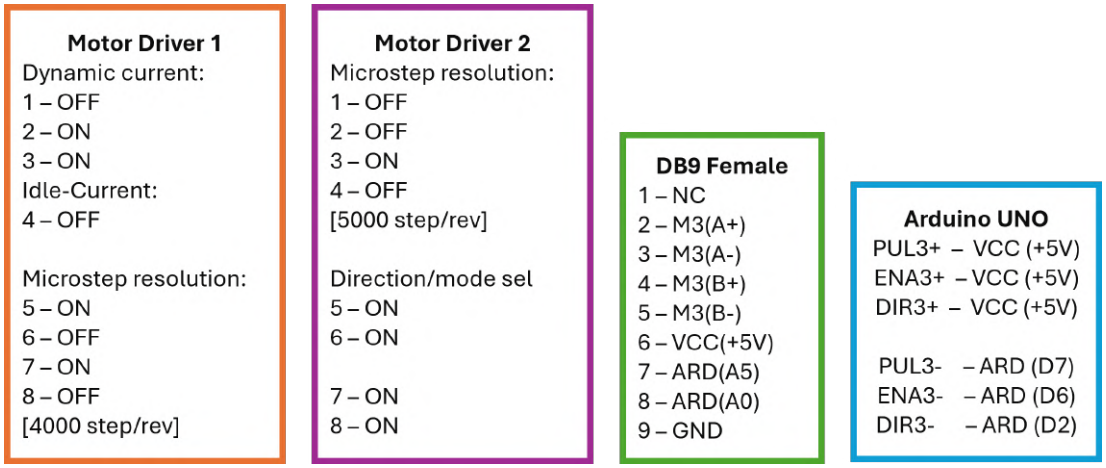

Figure 3.8: Overall pinout configuration

manageable units to obtain several benefits. For example, it allows the developer to separate basic functional and non-functional properties of the system [36]. Moreover, modularization helps to define the overall architecture in terms of relationships among modules, the so-called *architectural design* [37].

Independently of the specific crystal under test, each acquired frame is processed through the same high-level pipeline: image acquisition, conversion to an intensity representation, preprocessing/cleaning, and feature extraction for the subsequent geometric and statistical analysis.

Before describing the process for each crystal, some theoretical statistical methods used in these algorithms are introduced. Principal component analysis and Savitzky-Golay filter are the main techniques implemented to analyze the acquired images.

3.3.1 Principal Component Analysis

In recent years a large amount of data has become available and traditional measurements in areas such as particle physics are now performed with higher resolution and in substantially larger numbers. Such trends are now known as the “data deluge”; however, such vast quantities of data are of no great avail unless the relevant information they contain is appropriately extracted, a process known as *data mining*. Principal Component Analysis (PCA) is one of the well-established approaches for organizing and summarizing data [38].

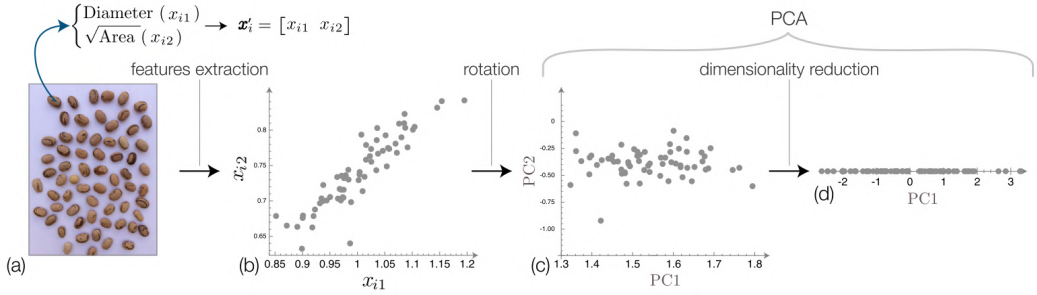

Figure 3.9: PCA example. Beans characterized by two features: diameter x_{i1} and square root of area x_{i2} [38].

Consider an object described by a feature vector $\mathbf{x}_i$ in an n-dimensional feature space. PCA can then be understood as a statistical method in which the coordinate axes of the feature space are rotated so that the first axis coincides with the direction of maximum data dispersion (as quantified by variance), the second axis with the direction of the second-largest dispersion, and so on. The PCA technique is mainly used to identify correlations between features and to simplify the original data with minimal loss of overall variance, enabling dimensionality reduction of the data. The reduction of dimensionality is obtained by projecting the data onto the directions of maximum data dispersion.

The case of a converted grayscale image represented as an intensity matrix corresponds to the $n = 2$ situation, the simplest to analyze and visualize. The features in that case are the coordinates of the pixels composing the image, so that they can be understood as a distribution of points in a two-dimensional space. The application of PCA to a two-dimensional space is illustrated in the example shown in Figure 3.9, where a set of beans is characterized in terms of their diameter x_{i1} and the square root of area x_{i2}. These two features are intrinsically related, and PCA allows the identification of the orientation of maximum data dispersion by rotating the system into the new axes PC1 and PC2. Finally, the resulting feature space can have dimension equal to one.

PCA can be understood as a linear transformation, expressible in the following matrix form:

$$Y = XW \tag{3.2}$$

where X is the $p \times n$ matrix containing n different features (random variables) and p

rows representing a *sample* of the random vector, and W is the *transformation matrix*. The derivation of W is described by the following steps:

- Calculation of the average of each variable:

$$\mu_{x_j} = \frac{1}{p} \sum_{i=1}^{p} x_{ij}$$

- Subtraction of the averages from the respective feature vectors:

$$\hat{\mathbf{x}}_j = \mathbf{x}_j - \mu_{x_j}$$

- Calculation of the *covariance matrix*:

$$K = \mathrm{Cov}(X) = \frac{1}{p-1} \widehat{X}^T \widehat{X}$$

  where $\widehat{X}$ is the matrix containing all the $\hat{\mathbf{x}}_j$ variables.

- Obtain the non-negative eigenvalues λ_j and their respective eigenvectors $\mathbf{w}_j$ of K by solving the linear equation

$$K\mathbf{w}_j = \lambda_j \mathbf{w}_j .$$

  Finally, the eigenvectors are combined as columns, in decreasing order of their eigenvalues, to obtain the transformation matrix W.

Once the transformation matrix W is obtained, the PCA projection is immediately computed using equation (3.2).

In the image-processing algorithms, PCA analysis is used to calculate the orientation of the data distribution with respect to the horizontal axis and to identify the centroid of an irregular reflective shape; more details are provided later.

3.3.2 Savitzky–Golay filter

Another technique implemented in the image-processing scripts is the Savitzky–Golay filter, one of the most widely used filters for smoothing and differentiating digital data.

It is derived by fitting a polynomial of degree m to each local window of $2k+1$ samples in the least-squares sense, and by evaluating the fitted polynomial at the window center. This least-squares regression can be expressed in matrix form and leads to a set of fixed convolution coefficients that are applied uniformly as a finite impulse response (FIR) filter across the dataset. This approach was first described by Savitzky and Golay (1964) [39].

For a given digital signal of N points and a given filter width w, the Savitzky–Golay filter computes a polynomial fit of order m in each filter window as the filter is moved across the signal [40].

The application of the Savitzky–Golay filter follows these steps:

- Let $\{y[n]\}_{n=0}^{N-1}$ be the original discrete dataset.
- For each element index n of the dataset, consider a symmetric window of length $2k+1$: $\{y[n-k], \ldots, y[n], \ldots, y[n+k]\}$.
- Inside each window, the data are approximated by a polynomial of degree m:

$$y[n+i] \approx a_0 + a_1 i + a_2 i^2 + \cdots + a_m i^m, \qquad i = -k, \ldots, k.$$

- The coefficients are obtained by minimizing the sum of squared residuals:

$$\min_{\mathbf{a}} \sum_{i=-k}^{k} \left(y[n+i] - \sum_{j=0}^{m} a_j \, i^j \right)^2,$$

  which in matrix form is written as $\mathbf{y} = \mathbf{X}\mathbf{a} + \boldsymbol{\epsilon}$.

- The solution to this linear system is given by the normal equations:

$$\hat{\mathbf{a}} = (\mathbf{X}^T\mathbf{X})^{-1}\mathbf{X}^T\mathbf{y},$$

  provided that $\mathbf{X}^T\mathbf{X}$ is invertible.

- The central value of each window, i.e. the value at index n, is the fitted polynomial

evaluated at the center ($i = 0$):

$$\hat{y}[n] = a_0.$$

Since $\hat{\mathbf{a}}$ depends linearly on $\mathbf{y}$, the output can be written as

$$\hat{y}[n] = \sum_{i=-k}^{k} c_i \, y[n+i],$$

where the coefficients c_i depend only on the window size and the polynomial degree.

Thus, the Savitzky–Golay filter is a linear finite impulse response (FIR) filter.

3.3.3 Processing workflow and implementation

The algorithms are implemented in Python, utilizing NumPy for array operations and numerical computations, together with scikit-learn and SciPy for statistical analysis of the intensity data. This implementation follows the modular design principles above, keeping algorithmic components and numerical libraries encapsulated within well-defined modules.

The processing chain for each image follows the same steps:

1. `main.py`: it works as the orchestreator of each modules.
2. `camera.py`: reading of the acquired image from the IDS camera.
3. `storage.py`: saving the image in a pandas array (3D, due to the camera RGB channels).
4. `IntensityMatrix.py`: converting the image into grayscale. This operation does not cause information loss because the acquired images are effectively black-and-white and the required information is the intensity matrix.
5. `crystal.py`: the intensity matrix is passed to the module tailored for the analyzed crystal.

3.3.4 Algorithms

Here the algorithms for each crystal are explained. Once the image is converted into an intensity matrix of pixels, each image is processed by different modules depending on the crystal type. This modular approach makes the software extensible: independently of the device under test, the system acquires images and converts them into intensity matrices, which are saved in `numpy` arrays and are ready to be processed by the corresponding *plug-in*. If additional processing is required for other crystals (for example, crystals with different shapes or different reflectivity), it is only necessary to implement the appropriate *plug-in* to analyze them.

RD22 crystal analysis algorithm

The RD22 crystals, introduced in Chapter 2, showed in figure 2.14, produce a characteristic image on the autocollimator that varies significantly with the applied curvature. Ideally, when no curvature is applied and the surface is perfectly planar, the image is rectangular because incident rays are reflected back perpendicular to the surface and the autocollimator magnification allows the entire crystal to be seen by the camera.

When the crystal is slightly bent, it begins to exhibit an hourglass-like profile: the widest regions correspond to locations where the anticlastic curvature is zero, and the narrowest regions correspond to locations where the anticlastic curvature is maximal. This assumption will be verified in the next chapters.

Because the bending is small in this regime, the whole crystal remains within the camera field of view. Experimental tests show that the crystal is fully illuminated and the reflected image represents the entire crystal: the test consists of covering an edge and observing a corresponding modification in the reflected image, thereby confirming that the reflected image originates from that edge.

When the bending becomes significant due to an increase in primary curvature, the reflected light is distributed over a larger angular range and some of it falls outside the autocollimator entrance aperture; the resulting image still has an hourglass-like appearance but extends beyond the captured frame. In that case the image requires a

different processing approach.

The imaging situations can be classified in three cases:

1. The crystal is fully within the camera field of view and the hourglass-like shape is entirely visible.
2. The curvature is sufficient that not all reflected light enters the autocollimator, but one end of the hourglass is still visible. In this case the hourglass appears "cut": the widest region is on the top and the narrowest on the bottom.
3. The symmetric case of (2), with the widest region on the bottom and the narrowest on the top.

Note that the crystal requires vertical alignment.

The algorithm converts the image in a 2D intensity matrix to extract the horizontal width profile along the vertical axis, identify the widest and narrowest sections, correct for tilt, and estimate curvature. The pipeline is deterministic and relies on robust preprocessing, PCA-based orientation, width extraction with directed scanning, trend detection via smoothed derivatives, and a geometric curvature estimate.

Preprocessing and intensity normalization

The algorithm input is a two-dimensional intensity matrix $I \in \mathbb{R}^{H \times W}$ representing the captured image of the crystal. To ensure consistent processing across images with varying exposure levels, the matrix is first normalized by its maximum value,

$$I_n = \frac{I}{\max(I)},$$

which maps intensities to the interval $[0, 1]$. This normalization is invalid if $\max(I) \leq 0$, which indicates an invalid or completely dark image.

Following normalization, a thresholding operation is applied to suppress background noise and low-intensity artifacts. Given a cleaning threshold τ_c (experimentally fixed

at $\tau_c = 0.4$), the cleaned matrix I_c is defined elementwise as

$$I_c(a,b) = \begin{cases} I_n(a,b), & \text{if } I_n(a,b) > \tau_c, \\ 0, & \text{otherwise,} \end{cases}$$

for $a = 1, \ldots, H$ and $b = 1, \ldots, W$. This operation effectively isolates the crystal footprint from the background while preserving intensity variations within the crystal region.

Tilt estimation via principal component analysis

Crystal orientation relative to the image axes is determined by PCA applied to the spatial distribution of non-zero pixels in the cleaned matrix. All pixel coordinates (x_i, y_i) for which $I_c(a,b) > 0$ are extracted and collected as a point cloud $\{(x_i, y_i)\}_{i=1}^{M}$. A two-component PCA decomposition is computed on this set of coordinates. The first principal component $\mathbf{v}_1 = [v_x,\ v_y]^\mathsf{T}$ represents the dominant axis of variation and corresponds to the major axis of the crystal footprint. For the RD22 crystal, which is expected to be vertically oriented, the tilt angle α is defined relative to the positive y-axis (vertical direction) and is computed as

$$\alpha = \arctan\left(\frac{v_y}{v_x}\right),$$

this angle allows to correct the *tilt error"* in the evaluation of the widest and narrowest length of pixels.

Width profile extraction

The core geometric measurement computes the horizontal width of the crystal at each vertical position. For each row $a \in \{0, 1, \ldots, H-1\}$, the algorithm identifies all column indices c where the cleaned intensity exceeds an edge-detection threshold τ_e. This threshold is an important parameter in this analysis, because it is the parameter able to individuate the edge of the crystal. Due to border effect, each crystal exhibits different fades near the border. Many variables define the border reflectivity: the

polishing-unpolishing of the crystal, that changes the reflectivity constant on the border, the perpendicularity of the cut, as well as misamtched in the crustal orientation. Nevertheless, thanks to empirical determination, a threshold is defined around 0.7 for the polished crystal. In general, grater the reflectivity, greater can be τ_e, in fact, the RD22 crystal, due to their high reflectivity and wide area, can be analysed even with a $\tau_e = 1$, but during the experiments, it has been evident that around an high value of τ_e the results doesn't change, because also the lenght of the zero-point (the widest row) changes its value by the same factor. Finally, the left edge L_a is defined as the minimum column index satisfying this condition, and the right edge R_a as the maximum. The width in pixels at row a is

$$w_a = R_a - L_a + 1$$

This process yields three arrays of length H: the width profile $\{w_a\}_{a=0}^{H-1}$, and the left and right edge positions $\{L_a\}_{a=0}^{H-1}$ and $\{R_a\}_{a=0}^{H-1}$. Subsequent analysis operates only on valid rows, i.e. those with finite width values.

Identification of extrema and directed scanning

Among all valid rows, the widest row $r_{\max}$ is identified as the position where the width profile attains its maximum value. This row is interpreted as the *"zero point"*, more precisely is the part of the crystal where the anticlastic curvature is null, thus, where the surface is assumed to be flat. To determine the narrowest rows, first of all the algorithm needs to identify where is it. As seen in figure 3.10 different images can occour. The narrowest section is identified by a "scanning" of the lengths of the rows, to determine which side to search, the algorithm compares $r_{\max}$ to the image midpoint $r_m = H/2$. If the widest row lies in the upper half ($r_{\max} < r_m$), the crystal is presumed to narrow toward the bottom and a downward scan (increasing row indices) is initiated. Conversely, if $r_{\max} > r_m$, an upward scan (decreasing row indices) is performed. This directed scanning strategy focuses the subsequent trend analysis on the relevant half of the crystal, avoiding ambiguity and improving robustness. The scan produces an ordered sequence of row indices and corresponding widths, denoted (r_i, w_i) for $i = 0, 1, \ldots, n-1$, where n is the number of valid rows on the selected side.

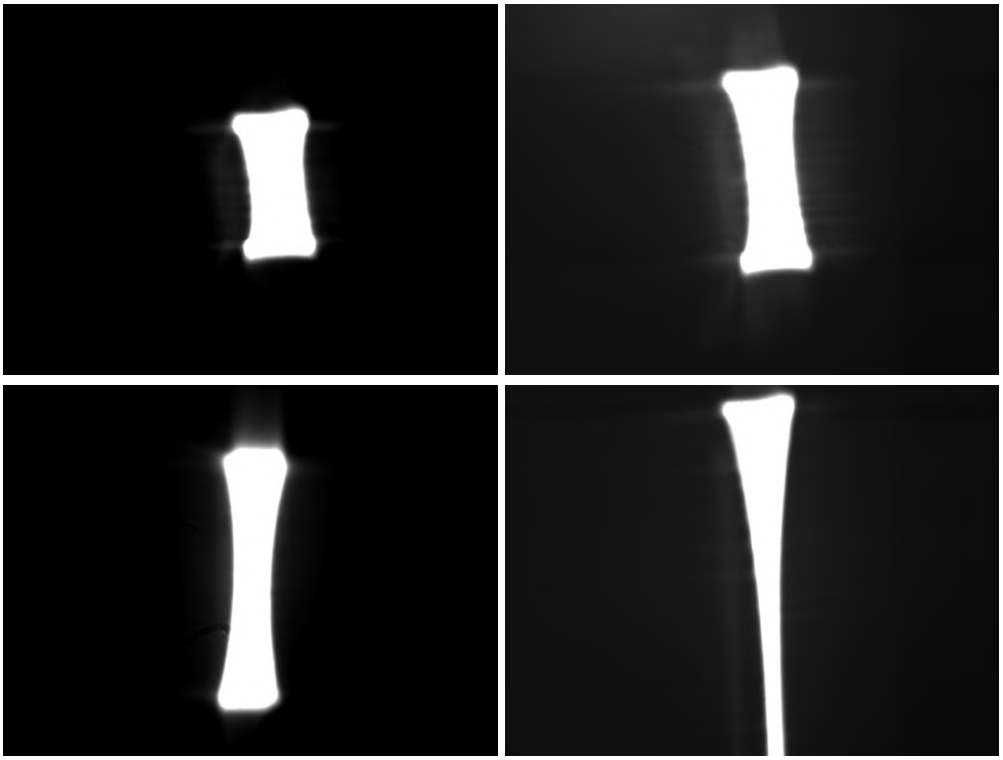

Figure 3.10: Crystals RD22 output for different progressive bending, starting from a quasi-zero bending to the maximum reached.

The scanned width sequence may exhibit one of two qualitative behaviors: a monotonic decrease (the crystal narrows uniformly) or a parabolic profile (narrowing followed by widening, characteristic of a symmetric hourglass). Distinguishing between these cases is critical for correctly identifying the narrowest point. The detection algorithm proceeds through smoothing, derivative computation, and transition search.

The raw scanned widths typically contain pixel-scale fluctuations due to discretization and intensity noise. To extract the underlying trend, the Savitzky–Golay filter is applied. As seen in the dedicated paragraph, the filter performs local polynomial regression over a moving window, smoothing the data while preserving features such as peaks and curvature better than a simple moving average. The polynomial order is set to 2 (quadratic), which is sufficient to capture parabolic behavior without overfitting noise. The window length is chosen adaptively as approximately 20% of the sequence length, computed as

$$\text{window} = \min\big(51,\ \max(9,\ 2\lfloor n/10 \rfloor + 1)\big),$$

ensuring an odd integer suitable for symmetric filtering. The bounds $[9, 51]$ prevent

degenerate cases: a minimum of 9 ensures enough points for a stable quadratic fit, while a maximum of 51 avoids excessive smoothing that would obscure real features. The filter is applied with `mode='interp'` to handle edges via interpolation, reducing boundary artifacts. The result is a smoothed sequence w_s.

To quantify the local trend, the discrete gradient $g = \nabla w_s$ is computed, approximating the derivative of the smoothed width profile. Positive gradient values indicate widening, negative values indicate narrowing, and near-zero values indicate a plateau. However, even after smoothing the gradient contains small fluctuations that do not represent meaningful changes.

A deadband threshold is then defined as

$$\varepsilon = \max\big(0.05,\ 0.1 \times \mathrm{MAD}(g)\big),$$

where $\mathrm{MAD}(g)$ denotes the median absolute deviation and the lower bound prevents excessively small thresholds. Gradient values within $[-\varepsilon, \varepsilon]$ are classified as ambiguous, values above ε as positive, and values below $-\varepsilon$ as negative. This produces a sign vector that separates increasing, decreasing, and flat regions.

The algorithm searches for a stable transition from negative to positive sign, which indicates the turning point in a parabolic profile, using a *stability window* of consecutive signs. If a transition is found, the trend is classified as parabolic and the narrowest point is expected near the transition: the index of the minimum smoothed width within the stability neighborhood is selected as the narrowest row. If no transition is detected, the trend is classified as monotonic and the narrowest row is the global minimum of the smoothed sequence. This dual strategy reduces the risk of selecting spurious minima (for example minima induced by border effects near flat zones) and improves robustness across different crystal shapes.

Measured widths are horizontal spans in pixel units; the true crystal width is corrected for tilt. For a vertically oriented crystal tilted by angle α from the vertical axis, the horizontal projection (measured width) is shorter than the true width by a factor $\cos\alpha$. To recover the true width, each measured width in pixels w_{px} is first converted to

micrometers by multiplying by the pixel size s (for the used camera $s = 4.5\ \mu$m/pixel):

$$w_{\mu\mathrm{m}} = w_{\mathrm{px}} \cdot s.$$

The tilt correction is then applied as

$$w^* = \frac{w_{\mu\mathrm{m}}}{|\cos\alpha|},$$

where α is the PCA-derived tilt angle. For valid cases, descriptive statistics (mean, median, standard deviation, minimum, maximum) are computed on the corrected width array, providing a summary of the crystal's dimensional characteristics.

Curvature angle estimation

The curvature of the crystal is quantified using the difference between the tilt-corrected widths at the widest and narrowest rows. Let w^*_{max} and w^*_{min} denote the tilt-corrected widths (in μm) at these extremal positions. The width difference

$$\Delta w = w^*_{\mathrm{max}} - w^*_{\mathrm{min}}$$

represents the maximum lateral deviation in the crystal profile (in μm).

Usin the autocollimator formula 2.1 and considering a focus length $f = 0.25\ m$, the measured angle is

$$\theta = \frac{\Delta w}{2f}\ \mu\mathrm{rad}$$

Output

The algorithm returns both arrays and metadata necessary for downstream analysis and validation:

- Processing parameters: thresholds (τ_c, τ_e), pixel size s, Savitzky–Golay parameters (window, poly order), deadband ε, stability window M.
- PCA results: tilt angle α, principal component vectors, number of points used.

- Scan direction, trend classification (parabolic or monotonic), widest and narrowest-row index.
- Row positions and corresponding widths $w^*_{\max}$, $w^*_{\min}$, and Δw.
- Curvature: $\theta_{\mu\text{rad}}$.
- Any error/warning flags produced during processing.

Strip crystal curvature analysis algorithm

The strip-crystal analysis pipeline supports two complementary measurement modalities for quantifying curvature: a secondary method based on width variations within a single image, and a primary method that tracks midpoint displacement across a sequence of images acquired at different positions along the crystal. Both approaches process two-dimensional intensity matrices acquired through optical imaging and employ principal component analysis for orientation estimation, robust statistical measures for noise suppression, and geometric models to convert measured deformations into curvature angles.

Both analysis modes begin with identical preprocessing steps showed in the previous paragraph about the RD22 crystals. The input intensity matrix is normalized to the interval $[0, 1]$ by dividing by its maximum value, then, a cleaned mask is exstracted, setting to zero all pixels below τ_c ($\tau_c = 0.4$). Crystal orientation relative to the image coordinate system is determined by PCA applied to the spatial distribution of nonzero pixels in the cleaned mask. For these crystals, which are expected to be horizontally oriented, the tilt angle α is obtained by taking the arctangent of the ratio between the vertical and horizontal components of the first principal component vector $v = (v_x, v_y)$, i.e.

$$\alpha = \arctan\left(\frac{v_y}{v_x}\right),$$

with α defined with the appropriate quadrant convention.

Secondary curvature analysis: *zero-point* method

The secondary method quantifies curvature through variations in the vertical width measured at sampled horizontal positions within a single image. This method adapts the RD22 hourglass approach to horizontally oriented strips.

In this approach the curvature is evaluated in a self-referenced way by introducing a *zero-point* (flat reference) measured on a flat region of the crystal. The measured vertical widths along the curved region are then expressed as differences with respect to this reference width, in order to remove offsets due to illumination, threshold choice and the finite apparent footprint of the crystal.

A dedicated reference image is acquired by aligning the crystal on an accessible flat region (the *zero* region). The normalized intensity matrix is then thresholded with a higher value than in the curved-region analysis, using $\tau_0 = 0.7$, i.e. all pixels with intensity ≤ 0.7 are set to zero. This choice is motivated by the fact that the flat part exhibits nearly maximal reflectivity and therefore saturates close to the normalized value 1.

On the resulting binary/cleaned mask, the vertical footprint height of the flat region is measured by extracting the central height of the illuminated blob, using the same robust definition adopted for the midpoint in the *midpoint-tracking method* (centroid/PCA projection and central-span estimation). The obtained reference height is stored as the zero-point width w_0 (in pixels).

To reduce computation and redundancy, columns are sampled at regular intervals defined by a step size (fixed at 10 pixels). Edge regions are excluded by skipping a margin of pixels from the left and right image borders (default 200 pixels each) to avoid boundary artifacts and mounting fixtures. For each sampled column c, row indices satisfying $I_c(r, c) > \tau_e$ (with τ_e typically 0.6–0.7) are identified. The first valid row r_{first} is the minimum satisfying this condition and the last valid row r_{last} is the maximum. The vertical width in pixels at column c is

$$w_c = r_{\text{last}} - r_{\text{first}} + 1.$$

The curvature-related width variation is then computed by subtracting the zero-point reference:

$$\Delta w_c = w_c - w_0.$$

Columns with no valid pixels are assigned NaN. The algorithm returns arrays of sampled column indices, raw widths w_c, zero-referenced widths Δw_c, and the first/last row positions for each sampled column.

Measured vertical widths are pixel spans; the zero-referenced width Δw_c is corrected for tilt using the angle computed by the PCA analysis, as in the RD22 algorithm. After conversion to micrometres, the tilt-corrected quantity is

$$\Delta w_c^* = \frac{\Delta w_{c,\mu\mathrm{m}}}{|\cos\alpha|}.$$

where α is the PCA-derived tilt angle.

Now, the autocollimator formula is applied

$$\theta_{\mu\mathrm{rad},i} = \frac{\Delta w_i^*}{2f} \quad (\mu\mathrm{rad})$$

The local radius of curvature is then

$$R_i = \frac{L_\mathrm{m}}{\theta_i}$$

where L_m is the characteristic crystal dimension in metres.

Primary curvature analysis: midpoint-tracking method

The primary method quantifies curvature by tracking a robust midpoint across a sequence of images acquired at regular spatial intervals along the crystal. This method captures global bending over extended crystal sections.

For each image, preprocessing (normalization, thresholding) is applied and nonzero pixel coordinates are extracted. PCA yields the local major axis $\mathbf{v}_1$ and centroid $\boldsymbol{\mu}$. To maintain a consistent coordinate system across images, a reference axis α_ref may be provided (from a global PCA or known alignment). The reference unit vector is

$\mathbf{u} = [\cos(\alpha_{\text{ref}}), \sin(\alpha_{\text{ref}})]$.

Pixel coordinates $\mathbf{p}_i$ are projected onto $\mathbf{u}$ relative to $\boldsymbol{\mu}$ by $s_i = (\mathbf{p}_i - \boldsymbol{\mu}) \cdot \mathbf{u}$, producing a one-dimensional distribution. In this case, not only is exploited the PCA for the alignment evaluation, but also to reduce the dimension of the distribution of the point. Two midpoint candidates are computed: the median $s_{\text{median}} = \text{median}(\{s_i\})$ and the extremal midpoint $s_{\text{ext}} = (s_{2\%} + s_{98\%})/2$ using the 2nd and 98th percentiles. The projected footprint length is $L_{\text{px}} = s_{98\%} - s_{2\%}$.

If $|s_{\text{median}} - s_{\text{ext}}| \leq 3$ pixels, the midpoint is averaged $s_{\text{mid}} = (s_{\text{median}} + s_{\text{ext}})/2$. Otherwise, the choice depends on the PCA variance ratio: for highly elongated footprints (variance ratio > 0.985) use s_{ext}; otherwise use s_{median}. The final midpoint in image coordinates is

$$\mathbf{p}_{\text{mid}} = \boldsymbol{\mu} + s_{\text{mid}}\mathbf{u},$$

yielding pixel coordinates $(x_{\text{mid}}, y_{\text{mid}})$.

Given a sequence of N images acquired at regular step intervals Δx (in millimetres), the midpoints $\mathbf{p}_{\text{mid}}^{(i)}$ are collected for valid images. Using the common projection direction $\mathbf{u}$, each midpoint is projected relative to the first midpoint:

$$t_i = (\mathbf{p}_{\text{mid}}^{(i)} - \mathbf{p}_{\text{mid}}^{(1)}) \cdot \mathbf{u}.$$

Consecutive displacements are $\Delta t_i = |t_{i+1} - t_i|$ (pixels), converted to micrometres $\Delta x_{\mu\text{m}} = \Delta t_i \cdot s$.

Applying the autocollimator formula, the curvature angle for each step is

$$\theta_i = \frac{\Delta x_{\text{m}}}{2f} \quad \text{(radians)},$$

The reported radius is obtained from the mean angle:

$$R_{\text{report}} = \frac{\Delta x_{\text{m}}}{\overline{\theta}},$$

where $\overline{\theta}$ is the mean of the θ_i values. The total accumulated curvature is $\Theta_{\text{total}} = \sum_i \theta_{\mu\text{rad},i}$ (in μrad).

Orchestration, output and metadata

High-level orchestration functions streamline processing. The secondary-analysis function processes a single image through preprocessing, PCA orientation, width extraction, tilt correction, and curvature calculation, returning processed arrays and metadata. The primary-analysis batch function processes sequences: it extracts midpoints (using a mandatory reference axis for consistency), collects valid midpoints, and computes sequence-based curvature metrics.

Both methods produce extensive outputs for validation and downstream analysis. Core arrays include the original, normalized, and cleaned images sampled column indices and width profiles in pixels and micrometres, row positions of width extremes and midpoint coordinates for sequence analysis. Metadata comprises processing parameters (τ_c, τ_e, s), PCA results (tilt angle, components, centroid), smoothing and detection parameters (Savitzky–Golay window and order, deadband ε, stability window M), trend classification, change index, extremal positions and widths, curvature angles and radii, coverage ratios, and any error or warning flags.

4 Measurements results

This chapter reports the experimental results and their metrological assessment. After a concise uncertainty analysis following metrological best practice, measurements obtained on strip and RD22 crystals are presented and compared across methods (autocollimator, optical profilometry and beam-based reconstruction). Emphasis is placed on the agreement between techniques, the repeatability of the autocollimator methods, and the interpretation of spatial curvature profiles such as the anticlastic gradient.

Uncertainty analysis

In metrology, measurement uncertainty accounts for the dispersion of values that can reasonably be attributed to a measurand. Following the GUM approach, uncertainty contributions are commonly classified into type A and type B components. Type A uncertainty is evaluated by statistical analysis of repeated observations (e.g., as a standard deviation or standard deviation of the mean) and therefore quantifies repeatability under the same measurement conditions. Type B uncertainty is evaluated by other means, such as instrument specifications, calibration certificates, resolution limits, manufacturer data, or previous characterization; it typically captures systematic or resolution-limited effects that are not estimated through repeated measurements. In the present work, both contributions are identified for each input quantity of the measurement model and then combined according to the law of propagation of uncertainty.

As seen in the chapter 2, the radius of curvature R is obtained from the measurement model

$$R = \frac{2fs}{\Delta y},$$

where f is the focal length of the optical system, s is the applied linear displacement of the translation stage, and Δy is the measured pixel displacement on the detector.

The uncertainty analysis was carried out by identifying both type A and type B contri-

butions.

The applied displacement s corresponds to the total translation imposed to the linear stage, typically in the range of 1 mm to 2 mm. The uncertainty on s was estimated considering the positioning accuracy of a stepper-motor-driven linear stage with a leadscrew of 4 mm pitch and microstepping. For millimetre-scale displacements, a conservative positioning accuracy of $\pm 1\,\mu$m was assumed, leading to a standard uncertainty

$$u(s) = \frac{1\,\mu\text{m}}{\sqrt{3}}, \tag{4.1}$$

corresponding to a relative uncertainty of approximately 0.06%.

The focal length f was measured using a digital caliper with a resolution of 0.01 mm. Assuming a rectangular distribution, the associated standard uncertainty is

$$u(f) = \frac{0.01\text{ mm}}{\sqrt{3}}, \tag{4.2}$$

which results in a negligible relative contribution ($\sim 0.006\%$ for $f \approx 100$ mm).

The pixel displacement Δy was determined using a fixed threshold criterion applied to the detector signal. Since the uncertainty is dominated by pixel quantization rather than statistical fluctuations, it was treated as a type B contribution. For the automated threshold-based algorithm, an uncertainty of ± 1 pixel was assumed, yielding

$$u(\Delta y) = \frac{1}{\sqrt{3}}\, p_{\text{px}}, \tag{4.3}$$

where $p_{\text{px}} = 4.5\,\mu$m is the pixel pitch. When the displacement was determined manually, a larger uncertainty of ± 5 pixels was considered.

The relative standard uncertainty on the radius of curvature due to type B contributions is given by

$$\left(\frac{u_B(R)}{R}\right)^2 = \left(\frac{u(s)}{s}\right)^2 + \left(\frac{u(f)}{f}\right)^2 + \left(\frac{u(\Delta y)}{\Delta y}\right)^2. \tag{4.4}$$

The analysis shows that the dominant contribution arises from the determination of the pixel displacement Δy, while the uncertainties associated with the mechanical displacement and the focal length are negligible in comparison. Since the uncertainty

on Δy is absolute and limited by pixel resolution, the relative uncertainty on R increases for large radii of curvature, corresponding to small angular deflections.

Repeated measurements were performed to estimate the statistical dispersion of the results, and the corresponding type A uncertainty was evaluated as the standard deviation of the mean. The combined standard uncertainty on R was finally obtained by quadratic summation of type A and type B contributions,

$$u(R) = \sqrt{u_A^2(R) + u_B^2(R)}. \tag{4.5}$$

For the zero-reference measurement method used to evaluate the anticlastic curvature, the curvature angle α is obtained directly from the measured displacement Δy through the autocollimator relation introduced in Chapter 2. In this case, Δy is defined as the difference between the image width corresponding to a flat reference region and that measured in the presence of curvature.

Since the measurement is based on the identification of the illuminated image borders on the detector, the uncertainty on Δy is dominated by the accuracy with which the edge position can be determined. This contribution is treated as a type B uncertainty, as it is mainly limited by pixel quantization and by the adopted edge-detection procedure.

The displacement Δy is obtained as

$$\Delta y = \Delta y_{\text{flat}} - \Delta y_{\text{curved}}, \tag{4.6}$$

where both terms are measured in detector pixels and subsequently converted into physical units using the known pixel pitch $p_{\text{px}} = 4.5\,\mu\text{m}$.

When an automated threshold-based algorithm is used to identify the image edges, an uncertainty of ± 1 pixel is assumed for both Δy_{flat} and Δy_{curved}. Assuming a rectangular distribution and uncorrelated contributions, the standard uncertainty on Δy is therefore

$$u(\Delta y) = \sqrt{u^2(\Delta y_{\text{flat}}) + u^2(\Delta y_{\text{curved}})} = \sqrt{2}\,\frac{1}{\sqrt{3}}\,p_{\text{px}}. \tag{4.7}$$

When the image borders are identified manually, a larger uncertainty of ± 5 pixels is

considered for each term, yielding

$$u(\Delta y) = \sqrt{2}\,\frac{5}{\sqrt{3}}\,p_{\mathrm{px}}. \tag{4.8}$$

Assuming a linear response of the autocollimator in the small-angle regime, the standard uncertainty associated with the curvature angle is obtained by propagation,

$$u(\alpha) = \left|\frac{\partial \alpha}{\partial \Delta y}\right| u(\Delta y), \tag{4.9}$$

where the sensitivity $\partial\alpha/\partial\Delta y$ depends only on the optical parameters of the autocollimator and is constant for a given configuration.

As for the primary curvature measurement, repeated acquisitions were performed to estimate the statistical dispersion of the results. The type A uncertainty was evaluated as the standard deviation of the mean, and the combined standard uncertainty on α was finally obtained as

$$u(\alpha) = \sqrt{u_A^2(\alpha) + u_B^2(\alpha)}. \tag{4.10}$$

The analysis shows that, also for the zero-reference method, the dominant contribution to the measurement uncertainty arises from the determination of the image borders on the detector, while other instrumental contributions are negligible in comparison.

4.1 Strip crystal measurements

4.1.1 Primary curvature

The primary curvature of the polished strip crystals was measured using two independent optical techniques: an autocollimator and a 3D optical surface profilometer (AltiSurf 520, provided by AlpyX, the crystal manufacturer). The comparison between the two measurements is reported in Table 4.1.

For Strip 1, the values obtained with the two techniques are consistent within the experimental uncertainty. The small discrepancy observed between the two measurements is of the same order as the estimated uncertainty budget and can therefore be

reasonably attributed to systematic effects intrinsic to the optical methods, such as alignment or interpolation uncertainties in the profilometer reconstruction. As a result, the measurement of the primary curvature for Strip 1 can be considered reliable.

In contrast, for Strip 2 a significantly larger discrepancy is observed between the autocollimator and profilometer measurements. This difference cannot be explained solely by the estimated measurement uncertainty. A plausible explanation is related to the mechanical configuration of the crystal: Strip 2 was bent with a lower tightening of the bending screw, resulting in a weaker mechanical constraint. Under these conditions, a partial relaxation of the applied curvature during transport between the two laboratories cannot be excluded. Indeed, the crystal was bent in the manufacturer's laboratory, located approximately 100 km from CERN, and was transported by car; the resulting handling and vibrations may have promoted a partial relaxation of the imposed curvature. Consequently, the primary curvature value measured for Strip 2 should be regarded as less reliable.

These observations highlight the sensitivity of the primary curvature to the mechanical boundary conditions imposed during bending, emphasizing the importance of stable and reproducible mounting conditions for accurate curvature characterization.

Table 4.1: Primary curvature radius measured for polished strip crystals using the autocollimator and a 3D optical profilometer.

Crystal	R_{AlpyX} [m]	R_{auto} [m]	$u(R_{\mathrm{auto}})$ [m]
Strip 1	0.905	0.939	±0.022
Strip 2	1.517	1.825	±0.059

4.1.2 Anticlastic curvature

The anticlastic curvature of the strip crystals was measured using the autocollimator through the zero-reference method described in Chapter 2. In this approach, the curvature is derived from the difference between the reflected image width corresponding to a flat reference region and that measured in the presence of anticlastic bending.

The measured anticlastic curvature angles for the two strip crystals are reported in Table 4.2. The curvature angle α is obtained from the measured radius assuming an

effective arc length of $L = 1$ mm, corresponding to the transverse dimension of the strip crystal along the anticlastic bending direction. The associated uncertainties were evaluated by combining the statistical dispersion of repeated measurements (type A) with the contribution due to the finite pixel resolution of the edge-detection algorithm (type B).

For both crystals, the uncertainty is dominated by the detector pixel resolution, while the statistical contribution is comparatively smaller, indicating good repeatability of the measurement procedure. The resulting curvature angles are of the order of a few hundred microradians, as expected for anticlastic bending induced by the applied primary curvature.

The autocollimator-based results are compared with independent beam-based measurements, which provide a direct estimate of the effective curvature experienced by the particle beam. A representative example of the beam measurement is shown in Fig. 4.1, where the deflection angle is reconstructed as a function of the transverse beam position. The beam-based measurements indicate curvature angles in the range 190–200 μrad for both crystals, in good agreement with the optical measurements.

Table 4.2: Anticlastic curvature angle of polished strip crystals.

Crystal	α_{beam} [μrad]	α_{auto} [μrad]	$u(\alpha_{\text{auto}})$ [μrad]
Strip 1	190	212	±6
Strip 2	200	193	±6

4.2 RD22 crystal measurements

4.2.1 Central anticlastic curvature

For the RD22 crystals, the anticlastic curvature represents the curvature responsible for beam deflection and is therefore the most relevant quantity to characterize. Measurements were performed at the crystal center, where the anticlastic curvature reaches its maximum due to the mechanical constraints imposed by the crystal holder. The results obtained during beam operation and from the autocollimator measurements performed after beam exposure are reported in Table 4.3.

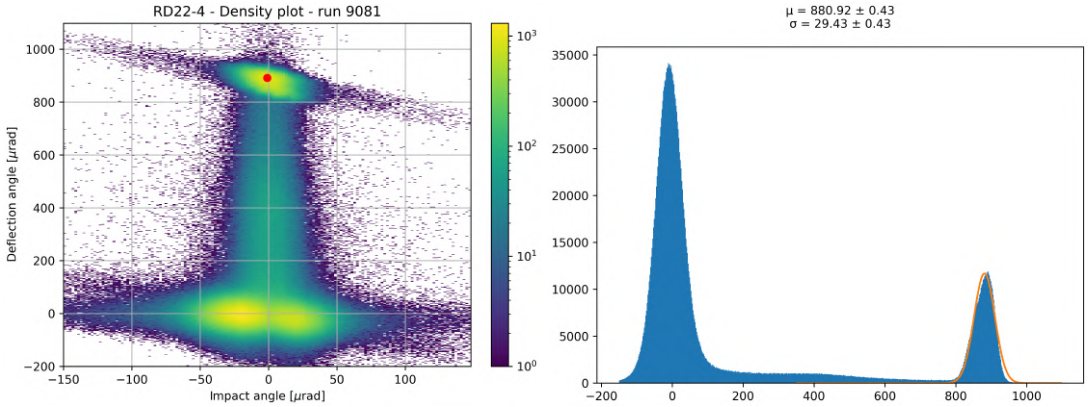

Figure 4.1: Example of beam-based measurement of the anticlastic curvature for a RD22 crystal. The deflection angle is reconstructed as a function of the transverse beam position. Then a gaussian fit is computed on the channelled particles, represented as counts in fuction of the deflection angle. Finally, the angle of curvature, corresponding to the particles deflection, is computed ad the average value of the gaussian fit.

For RD22–4, the anticlastic curvature measured with the autocollimator is consistent with the beam-based value within the experimental uncertainty, indicating negligible changes due to handling and operation. Similarly, RD22–3 shows a close agreement between beam-based and optical measurements, with the observed difference remaining small compared with the corresponding curvature magnitude. Overall, the results suggest that the mechanical clamping and transport conditions were sufficiently stable for both crystals, and that the post-exposure autocollimator measurements provide a reliable estimate of the curvature during beam operation.

Table 4.3: Anticlastic curvature angle measured at the center of RD22 crystals.

Crystal	α_{beam} [μrad]	α_{auto} [μrad]	$u(\alpha_{\text{auto}})$ [μrad]
RD22–3	-1500	-1575	±6.7
RD22–4	-950	-1012.5	±6.2

4.2.2 Anticlastic curvature gradient

A detailed scan of the anticlastic curvature along the vertical direction was performed for the RD22-4 crystal using both the beam-based measurement and the autocollimator. The measured curvature exhibits a clear parabolic profile as expected, with values close to zero at the upper and lower edges and a maximum located near the crystal center.

This behavior reflects the mechanical constraints imposed by the crystal legs, which enforce flatness at the boundaries while allowing elastic flexure in the central region.

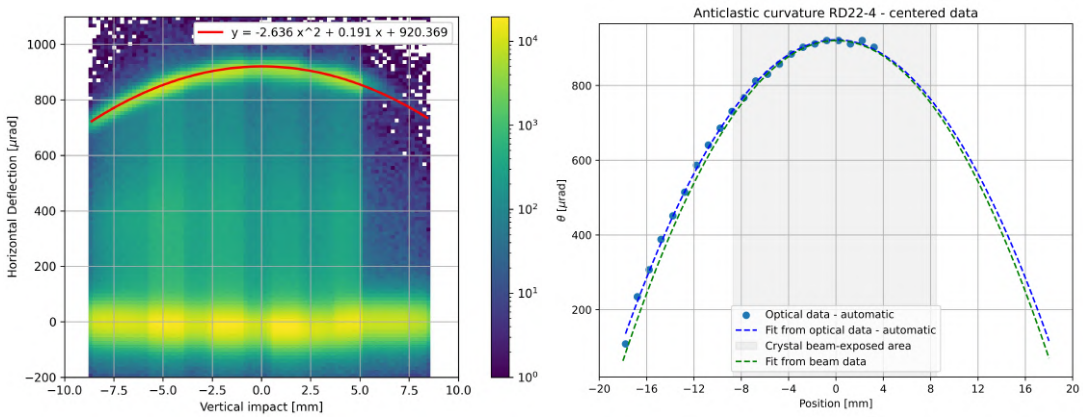

Figure 4.2: RD22 crystal anticlastic curvature gradient. *Left*: plot of horizontal particle deflection versus vertical impact position, obtained by combining multiple runs at different crystal heights; the red line shows the fitted curvature gradient. *Right*: comparison between the fit from beam data and the fit from optical data.

The main parameters describing the curvature gradient are summarized in Fig. 4.2. The left panel shows the curvature profile reconstructed from several beam runs combined together. During the measurement, the crystal was scanned along the vertical direction by means of an automated translation stage, with a step size of 3 mm. For each vertical position, the deflection angle was reconstructed, allowing the curvature profile to be sampled over the full height of the crystal.

The resulting profile exhibits the characteristic parabolic shape expected for anticlastic bending under the mechanical constraints imposed by the crystal holder. A parabolic fit (red line) is superimposed on the data, and the corresponding analytical expression is explicitly reported in the figure. This fit provides a quantitative description of the curvature gradient and allows the extraction of the relevant parameters for comparison with the optical measurements.

The right panel of Fig. 4.2 shows the superposition of the parabolic fits obtained from the beam-based reconstruction and from the autocollimator measurements. The two curves are plotted on the same axes and are found to be very close to each other over the full vertical range, demonstrating a high level of consistency between the two independent measurement techniques.

To quantify the discrepancy between the two curves, the second-order polynomial fits were compared over the common measurement span $x \in [-9, 9]$ mm. Although the new-instrument data are displayed over a wider interval (from -20 to 20 mm), the reference measurements were acquired only within $[-9, 9]$ mm; therefore, the analysis was restricted to this overlap region to avoid extrapolation and to ensure that the comparison is based exclusively on measured data. The assessment was performed on the pointwise difference between the fitted models, $\Delta(x) = p_2(x) - p_1(x)$, which reads $\Delta(x) = -0.147\,x^2 + 0.191\,x - 2.041$.

Since a single indicator cannot fully describe both typical and worst-case deviations, three complementary metrics were used:

- the span-averaged difference (bias)

$$\overline{\Delta} = \frac{1}{L} \int_{-9}^{9} \Delta(x)\, dx,$$

  yielding $\overline{\Delta} = -6.01$ μrad, which captures the *mean signed shift* between the two profiles across the whole overlap region. A nonzero bias indicates that one method produces, on average, systematically larger (or smaller) curvature angles than the other, as would be expected from a constant calibration or alignment offset; however, it does not describe how the discrepancy varies with position;

- the root-mean-square deviation

$$\mathrm{RMS} = \sqrt{\frac{1}{L} \int_{-9}^{9} \Delta(x)^2\, dx},$$

  yielding RMS $= 8.29$ μrad, which represents the *overall typical disagreement* by weighting all pointwise differences and removing the sign. Unlike the bias, the RMS is sensitive to both a global offset and position-dependent deviations; it therefore summarizes the combined effect of systematic and local mismatches into a single "average error" magnitude;

- the maximum absolute deviation

$$E_{\max} = \max_{x \in [-9,9]} |\Delta(x)|,$$

yielding $E_{\max} = 15.69$ μrad (at $x = -9$ mm), which provides a *worst-case indicator* of the discrepancy over the comparison span. This metric is dominated by the largest local departure between the fits (often near the interval boundaries), making it particularly relevant when the comparison is used to bound the maximum possible error at any position rather than the average behavior.

Finally, To separate a pure offset from a residual shape mismatch, the bias-corrected

$$\mathrm{RMS}_{\mathrm{form}} = \sqrt{\frac{1}{L} \int_{-9}^{9} \left(\Delta(x) - \overline{\Delta} \right)^2 \, dx}$$

was also computed, resulting in $\mathrm{RMS}_{\mathrm{form}} = 5.70$ μrad.

This agreement confirms the capability of the optical method to accurately reproduce not only the maximum anticlastic curvature but also its spatial gradient along the crystal.

Overall, the results show good agreement between the autocollimator-based measurements and the beam-based characterization.

Conclusions

In this thesis an automated optical system based on an autocollimator has been developed and applied to the characterization of bent silicon crystals used in crystal-assisted beam collimation experiments. The work addresses the need for a precise, non-destructive and laboratory-accessible method capable of measuring both primary and anticlastic curvature components of small crystals, which play a crucial role in particle channeling phenomena. The operating principles of bent crystals and of conventional curvature measurement techniques were reviewed to provide the physical and experimental context of the study. An autocollimator-based approach was then proposed and implemented, exploiting its high angular sensitivity and non-contact nature. Dedicated measurement procedures were designed for different crystal geometries, and a fully automated acquisition chain was realized through the integration of motorized translation stages and custom software.

The development of tailored image-processing algorithms proved essential to extract reliable curvature information from the autocollimator images. The use of filtering and statistical techniques significantly improved measurement stability and repeatability, especially for thin strip crystals, where anticlastic effects are particularly relevant.

The comparison with beam-based curvature measurements performed at CERN demonstrates that the optical system achieves an accuracy compatible with the requirements of the UA9 experimental program. In particular, for strip crystals the primary curvature radius was measured with deviations below 7% (Strip 1) and within 10% (Strip 2), with relative standard uncertainties below 4%, while the anticlastic curvature angles agree with the beam-based reference within $\pm 22\,\mu$rad with a standard uncertainty of $6\,\mu$rad. For RD22 crystals, the automated system reproduced the central anticlastic curvature within 5% of the beam-based characterization and captured the anticlastic curvature gradient with good consistency: over the common span $x \in [-9, 9]$ mm the discrepancy

between the two parabolic fits corresponds to a bias of $-6.01\,\mu$rad, an RMS deviation of $8.29\,\mu$rad, and a maximum absolute deviation of $15.69\,\mu$rad. The results confirm the validity of the proposed method as a powerful tool for crystal pre-characterization and quality control, enabling systematic studies to be carried out independently of accelerator availability.

The measurement method and the automated system developed in this work have also led to the preparation of a scientific article describing the approach and the corresponding experimental validation [41].

Future developments of the system may focus on further improving measurement stability, optical efficiency, and alignment reproducibility. In particular, the adoption of a more stable and precise optical translation system would reduce mechanical uncertainties and enhance repeatability during automated scans. Significant improvements could also be achieved by refining the preliminary laser-based optical alignment procedure, for instance through the use of reference gratings and polarized beam splitters, enabling a more robust and reproducible definition of the optical axis. From an optical design perspective, the use of an achromatic doublet lens with larger diameter and higher magnification represents a promising upgrade. A larger aperture would allow the collection of a greater fraction of the reflected light, especially for large reflection angles, while increased magnification would result in more expanded images on the detector. This combination would improve both signal-to-noise ratio and angular resolution, extending the operational range and overall performance of the measurement system.

Bibliography

[1] European Organization for Nuclear Research (CERN). *CERN Accelerating science — Home*. https://home.cern/. 2026.

[2] Werner Herr. "431–459 Herr: Review of Accelerator Physics at CERN". In: *CERN CDS* (2013). URL: https://cds.cern.ch/record/1982430/files/431-459%20Herr.pdf.

[3] European Organization for Nuclear Research (CERN). *HiLumi LHC*. https://home.cern/science/accelerators/hilumi-lhc. Consultato il 24 febbraio 2026. 2026.

[4] E. N. Tsyganov. *Some aspects of the mechanism of charged particle penetration through a monocrystal*. Fermilab TM-682. Fermilab, 1976.

[5] J. Lindhard. "Influence of crystal lattice on motion of energetic charged particles". In: *Matematisk-Fysiske Meddelelser, Dan. Vid. Selsk.* 34.14 (1965), pp. 1–64.

[6] U. I. Uggerhøj. "The interaction of relativistic particles with strong crystalline fields". In: *Reviews of Modern Physics* 77 (2005), pp. 1131–1171. DOI: 10.1103/RevModPhys.77.1131.

[7] V.M. Biryukov et al. "Crystal collimation as an option for the large hadron colliders". In: *Nuclear Instruments and Methods in Physics Research Section B* 234 (2005), pp. 23–30. DOI: 10.1016/j.nimb.2005.03.003.

[8] V. M. Biryukov, Y. A. Chesnokov, and V. I. Kotov. *Crystal Channeling and its Application at High-Energy Accelerators*. Berlin: Springer, 1997.

[9] Charles Kittel. *Introduction to Solid State Physics*. 8th ed. New York: John Wiley & Sons, 2005.

[10] W. Scandale et al. "Overview of crystal-assisted beam steering and collimation studies". In: *Journal of Instrumentation* 11.C09005 (2016). Review / proceedings-style overview; useful for experimental context, pp. 1–14.

[11] L. D. Landau and E. M. Lifshitz. *Theory of Elasticity*. 3rd ed. Pergamon Press, 1986.

[12] W. Scandale and A. M. Taratin. "Channeling and volume reflection of high-energy charged particles in short bent crystals. Crystal assisted collimation of the accelerator beam halo". In: *Physics Reports* 815 (2019), pp. 1–107. DOI: 10.1016/j.physrep.2019.04.003.

[13] D. S. Gemmell. "Channeling and related effects in the motion of charged particles through crystals". In: *Reviews of Modern Physics* 46.1 (1974), pp. 129–227. DOI: 10.1103/RevModPhys.46.129.

[14] W. Scandale et al. "High-Efficiency Volume Reflection of an Ultrarelativistic Proton Beam with a Bent Silicon Crystal". In: *Physical Review Letters* 98.15 (2007), p. 154801. DOI: 10.1103/PhysRevLett.98.154801.

[15] Walter Scandale et al. "Crystals to Assist the Two-Beam Merging Process in the UA9 Apparatus". Manuscript submitted to *Journal of instrumentation*, unpublished. 2025.

[16] B. D. Cullity. *Elements of X-Ray Diffraction*. 2nd ed. Reading, MA: Addison-Wesley, 1978.

[17] Pablo Serrano Galvez and Yury Gavrikov. *Instrumentation and Procedures to Test Bent Silicon Crystals with X-Rays at CERN*. Tech. rep. Geneva: CERN, 2020. URL: https://cds.cern.ch/record/2730428.

[18] M. Hart and J. R. Gao. "Radii of curvature from X-ray diffraction with a one-dimensional detector". In: *Nuclear Instruments and Methods in Physics Research Section A* 310.1–2 (1991), pp. 326–334. DOI: 10.1016/0168-9002(91)90723-U.

[19] B. K. Tanner and P. A. Midgley. "Metrology of warpage in silicon wafers using X-ray diffraction mapping". In: *Journal of Applied Physics* 71.9 (1992), pp. 4280–4285. DOI: 10.1063/1.350761.

[20] Altimet. *AltiSurf 520: High Precision Optical Surface Profiler*. https://www.altimet.fr/?page_id=236&lang=en. Technical specifications and product description. 2023.

[21] AlpyX. *AlpyX – Bent Crystals for Beam Steering Applications*. https://www.alpyx.fr/. Company website. 2024.

[22] Eugene Hecht. *Optics*. 5th ed. London: Pearson, 2017.

[23] Moeller-Wedel Optical GmbH. *Examples for Applications of collimators, telescopes, visual and electronic autocollimators*. Tech. rep. Moeller-Wedel Optical GmbH, 2013.

[24] National Physical Laboratory. *Guide to Angular Measurement: Autocollimators and Angular Metrology*. Tech. rep. Technical guide on principles and calibration practices. NPL, 2010.

[25] *CCM1-BS013/M Broadband Beamsplitter Cube - Technical Information*. Product technical information and specifications. Thorlabs. 2018.

[26] Joseph W. Goodman. *Introduction to Fourier Optics*. 3rd ed. Tucson, AZ: Roberts & Company Publishers, 2005.

[27] *U3-36P0XLE-M-GL Rev.1.2 (1011191)*. Datasheet, subject to technical modifications (2025-11-18). IDS Imaging Development Systems GmbH. Dimbacher Str. 10, 74182 Obersulm, Germany, 2025. URL: https://www.ids-imaging.com.

[28] *EO-2018 LE Monochrome USB 3.0 Lite Edition Camera, #89-735*. Model EO-2018 LE / UI-3250, subject to technical modifications (16-09-2025). Edmund Optics Inc. 101 E Gloucester Pike, Barrington, NJ 08007, USA, 2025. URL: https://www.edmundoptics.com.

[29] James Janesick. *Scientific Charge-Coupled Devices*. Bellingham, WA: SPIE Press, 2001.

[30] Yi-Ting Tu et al. *Ray Optics Simulation*. https://phydemo.app/ray-optics/simulator/. Web-based ray optics simulator. PhyDemo, 2025. URL: https://phydemo.app/ray-optics/simulator/.

[31] The RD22 Collaboration. *Status Report on RD22: Crystal Extraction at the SPS*. Tech. rep. CERN/DRDC 92-51. RD22 Status Report. Geneva, Switzerland: CERN, Oct. 1992.

[32] The RD22 Collaboration. *Second Status Report on RD22: Crystal Extraction at the SPS*. Tech. rep. CERN/DRDC 94-11. RD22 Status Report. Geneva, Switzerland: CERN, Mar. 1994.

[33] Andrii Natochii et al. *Motorized linear stages for the UA9 experiment*. Tech. rep. Geneva: CERN, 2019. URL: https://cds.cern.ch/record/2676024.

[34] *23Y Series - High Torque Stepper Motors*. 23Y004S-LW4. Anaheim Automation. 2012.

[35] Leadshine Motion Technology. *EM503 2-Phase Digital Stepper Drive Datasheet*. Version 1.0, December 10, 2015. Leadshine Motion Technology. 2015.

[36] Aseem Daga, Sergio de Cesare, and Mark Lycett. "Separation of Concerns: Techniques, Issues and Implications". In: *Journal of Intelligent Systems* 15.1–4 (2006), pp. 153–175.

[37] Carlo Ghezzi, Mehdi Jazayeri, and Dino Mandrioli. *Fundamentals of Software Engineering*. 2nd ed. New Delhi: Prentice-Hall, 2003.

[38] Felipe L. Gewers et al. "Principal component analysis: A natural approach to data exploration". In: *ACM Computing Surveys* 54 (4 May 2022). ISSN: 15577341. DOI: 10.1145/3447755.

[39] Literature Cited ; Cohen et al. *Smoothing and Differentiation of Data by Simplified Least Squares Pro,cedures*. Tech. rep. The Perkin-Elmer Corp., Norwalk, Conn, 1964.

[40] Neal B Gallagher. *Savitzky-Golay Smoothing and Differentiation Filter*. Tech. rep. Eigenvector research incorporated, 2020. URL: www.Eigenvector.com.

[41] W. Scandale et al. "Bent crystal characterization from Autocollimator measurements". In: *Journal of Instrumentation* 21.03 (2026), P03026. DOI: 10.1088/1748-0221/21/03/P03026.

List of Figures

List of Tables